GEOLOGY

Submarine ash megabed fed by far-traveled, shoreline-crossing pyroclastic currents from a large explosive volcanic eruption

Abigail Metcalfe^{1*}, Tim Druitt¹, Katharina Pank², Steffen Kutterolf², Jonas Preine³, Karim Kelfoun¹, Christian Hübscher³, Paraskevi Nomikou⁴, Thomas A. Ronge⁵, Shun Chiyonobu⁶, Olga Koukousioura⁷, Adam Woodhouse⁸, Sarah Beethe⁹, Michael Manga¹⁰, Iona McIntosh¹¹, Masako Tominaga¹², Carole Berthod¹³, Hehe Chen¹⁴, Acacia Clark¹⁵, Susan DeBari¹⁶, Ralf Gertisser¹⁷, Raymond Johnston¹⁸, Ally Peccia¹⁹, Yuzuru Yamamoto²⁰, Alexis Bernard²¹, Tatiana Fernandez Perez²², Christopher K. Jones²³, Kumar Batuk Joshi²⁴, Günther Kletetschka^{25,26}, Molly McCanta²⁷, Antony Morris²⁸, Paraskevi Polymenakou²⁹, Xiaohui Li³⁰, Jean-Marie Nedelec³¹, Hao-Yang Lee³², Dimitrios Papanikolaou⁴

Large explosive volcanic eruptions from island volcanoes deliver vast quantities of ash to the marine environment. While many of the transport pathways are understood, those from shoreline-crossing or submarine pyroclastic currents, and their transformation into water-supported gravity flows, remain poorly constrained. We report the discovery by International Ocean Discovery Program (IODP) deep drilling of a 200-meter-thick ash megabed buried in rift basins of the South Aegean Volcanic Arc. The >73-cubic kilometer ash deposit originates from the Kos Plateau Tuff caldera-forming eruption, which occurred 161 thousand years ago, >120 kilometers to the east. The ash forms a chemically uniform, graded megabed lacking bioturbation, interpreted as having been emplaced by a stream of eruption-fed turbidity currents. Bioclastic debris within the ash provides evidence of widespread destruction of marine ecosystems. Large volcanic eruptions can remodel the seafloor landscape, deposit thick ash turbidites, and destroy marine biota on island arc-wide scales in short-lived, catastrophic events.

Copyright © 2025 The Authors, some rights reserved; exclusive licensee American Association for the Advancement of Science. No claim to original U.S.
Government Works.
Distributed under a Creative Commons Attribution
NonCommercial
License 4.0 (CC BY-NC).

INTRODUCTION

Explosive volcanic eruptions produce ash by the violent fragmentation of gas-charged magma (1). The fine particle sizes (<2 mm) and low settling velocities in water (relative to the speeds of marine currents) result in wide dispersal of volcanic ash in the marine environment (2), significantly affecting ecosystems, biogeochemical cycles (3), and submarine cable networks (4). Some common mechanisms by which ash enters the oceans include submarine eruptions (5), fallout from Plinian eruption columns (6), attrition of pumice rafts (7), sedimentation from sea-surface pyroclastic currents (8-12), and fallout from atmospheric coignimbrite ash ("Phoenix") plumes (13). The last mechanism involves buoyant lofting of ash and hot gases

from subaerial pyroclastic currents (traveling across land or sea), potentially accounting for a substantial fraction of the total erupted volume (13). These processes, all observable in nature and well understood (2), result in ash layers in marine sediments that are crucial for tephrochronology and for estimating the volumes of explosive eruptions (14).

The fate of the huge volumes of ash that enter the ocean in the form of dense, seafloor-hugging pyroclastic currents, which then entrain water and transform into debris flows, granular slurries, and turbidity currents, is more enigmatic (15–22). The processes and submarine products arising from the entry of pyroclastic currents into the sea have been studied using ancient examples (15, 16, 19),

¹University Clermont-Auvergne, CNRS, IRD, OPGC, Laboratoire Magmas et Volcans, Clermont-Ferrand, France. ²GEOMAR Helmholtz Centre for Ocean Research Kiel, Wischhofstrasse 1-3, D-24148 Kiel, Germany. ³Institute of Geophysics, University of Hamburg, Bundesstrasse 55, D-20146 Hamburg, Germany. ⁴Department of Geology and Geoenvironment, National and Kapodistrian University of Athens, 15784 Athens, Greece. ⁵International Ocean Discovery Program, Texas A&M University, College Station, TX 77845, USA. ⁶Faculty of International Resource Sciences, Akita University, Akita, Akita Prefecture 0108502, Japan. ⁵School of Geology, Aristotle University of Thessaloniki, 54124 Thessaloniki, Greece. ⁸Institute for Geophysics, University of Texas, J.J. Pickle Research Campus, Bldg. 196, Austin, TX 78758, USA. ⁹College of Earth, Ocean, and Atmospheric Sciences, Oregon State University, Corvallis, OR 97333, USA. ¹⁰Department of Earth and Planetary Science, University of California, Berkeley, CA 94720, USA. ¹¹Japan Agency for Marine-Earth Science and Technology, 2-15 Natsushima-cho, Yokosuka, Kanagawa 237-0061, Japan. ¹²Department of Geology and Geophysics, Woods Hole Oceanographic Institution, Woods Hole, MA 02543, USA. ¹³Institut De Physique Du Globe De Paris, Centre National de la Recherche Scientifique (CNRS), 75005 Paris, France. ¹⁴School of Ocean Sciences, China University of Geosciences, Haidan District, 100083 Beijing, China. ¹⁵School of Reography, Geology and the Environment, Keele University, Keele, Staffordshire ST5 5BG, UK. ¹⁸School of Geosciences, University, Bellingham, WA 98225, USA. ¹⁷School of Geography, Geology and the Environment, Keele University, Palisades, NY 10964, USA. ²⁶Craduate School of Science, Kobe University, 1-1 Rokkodai-cho, Nada-ku, Kobe, Hyogo 657-8501, Japan. ²¹Laboratoire des Fluides Complexes et leurs Réservoirs, Université de Pau et des Pays de l'Adour, F-64000 Pau, France. ²²Department of Geology, Kent State University, 221 McGilvrey Hall, 325 S Lincoln Stre

modern examples (4, 23), and laboratory experiments (17, 19), with comprehensive reviews published [(16, 24, 25) and the references therein]. One school of thought has been that dense pyroclastic currents can retain their heat for large distances under water. Supporting this idea, the submarine ignimbrite (massive, pumice-rich deposit from a pyroclastic current) from the Krakatau 1883 eruption was emplaced at temperatures of 475° to 550°C as far as 15-km offshore from the island (26), either because the highly concentrated basal levels of the current had entrained little seawater or because there had been insufficient time for the pyroclasts to cool. However, most studies infer that pyroclastic currents rapidly entrain seawater and transform into cold subaqueous density flows, either progressively during transport or due to explosive mixing in the littoral zone (24). A particularly well-documented modern example is the 2022 eruption of the partially submerged Hunga Volcano, which discharged fast-moving (exceeding 120 km hour⁻¹) pyroclastic currents by column collapse into the Pacific Ocean, scouring the seafloor, and laying down volcaniclastic sediment to over 100 km from source (4, 23). However, although the volume of the Hunga-Tonga deposits is ~6 km³, some terrestrial explosive eruptions discharge many hundreds or even thousands of cubic kilometers of ash in the form of pyroclastic currents (27). The entry of such pyroclastic currents into the sea can form submarine megabeds (unusually thick and laterally extensive beds that differ in composition from the host sediments) of volcaniclastic material (24). Submarine volcaniclastic megabeds generated directly by eruptions are distinguished from those produced by other mechanisms, such as volcanic flank collapses by an abundance of chemically homogeneous juvenile components (20, 24). While ancient examples of eruption-generated submarine megabeds

have been described, the source conditions are commonly unknown (16, 24, 25). Moreover, the processes of hydraulic sorting of particles of different sizes and densities in submarine volcaniclastic flows and the distal fate of the fine components remain poorly constrained. We address this knowledge gap via the deep drilling of a 200-m-thick ash megabed from the Kos Plateau Tuff (KPT) caldera-forming eruption on the South Aegean Volcanic Arc. Through a combination of sedimentological characterization, core-seismic integration, and numerical modeling, we unravel the processes that gave rise to this enormous submarine deposit.

The KPT eruption took place 161,000 ± 2000 years ago from the Kos caldera complex in the eastern part of the South Aegean Volcanic Arc (28, 29) (Fig. 1). The eruption succession has been reconstructed from detailed studies of onland deposits (30). The eruption discharged a total of over a hundred cubic kilometers of biotitebearing rhyolitic pumice and ash in a six-phase (A to F), waxing-towaning sequence lasting several hours to several days (30). Onland unit A consists of a phreatomagmatic fall deposit, while units B to F consist of pyroclastic current deposits. The climactic phase of the eruption is represented by unit E, when the peak discharge rate is estimated from numerical modeling to have been 4×10^9 to 8×10^9 10^9 kg s^{-1} (11). On the basis of isopach, isopleth, and transport direction data, the eruption is inferred to have taken place from one or more vents south of Kos (Fig. 1) and to have formed a caldera 10 to 20 km in diameter (30). The pyroclastic currents of the eruption were generated by column collapse (30). To the north, they traveled across land to deposit on Kos, Kalymnos, Pserimos, and the Bodrum Peninsula. To the south and east, they traveled across either shallow water (10) or land (31) to deposit on Tilos, Chalki, and the Datça

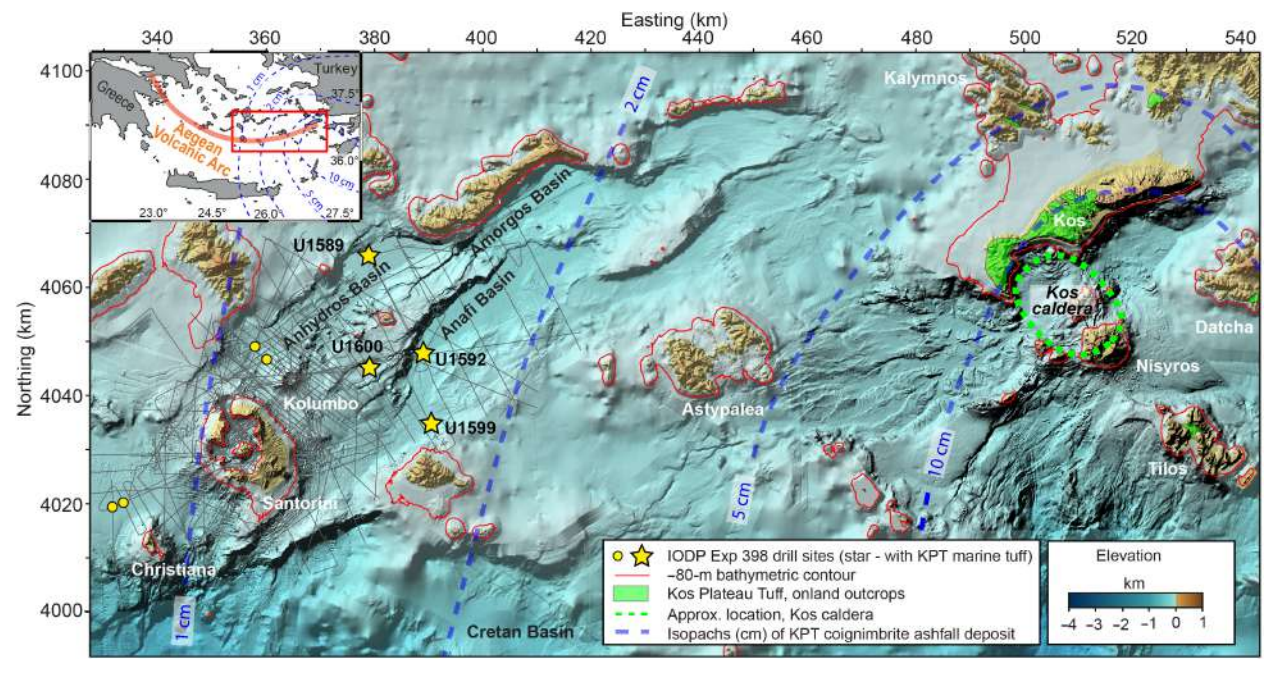


Fig. 1. Shaded bathymetric map of the eastern half of the South Aegean Volcanic Arc. The red rectangle on the inset locates the main figure. IODP Expedition 398 drill sites outside of Santorini caldera are marked with yellow symbols and their IODP site numbers (those inside the caldera are not shown). Sites where the Kos Plateau Tuff (KPT) submarine megabed was intersected are shown as stars. Present-day water depths at these sites are 484 m (Site U1589), 693 m (Site U1592), 592 m (Site U1599), and 326 m (Site 1600). The distribution of onland outcrops of the 161 ka KPT is shown in green, along with the approximate location of the Kos caldera (30). Isopachs for the KPT coignimbrite ash fall are shown on the main map and inset (14). At the time of the eruption, sea level was about 80 m below the present-day level; the -80-m bathymetric contour is shown in red. The gray lines are published seismic profiles.

Peninsula (Fig. 1). The submarine deposits from the KPT pyroclastic currents have been tentatively recognized in seismic profiles around the Kos caldera (29, 31, 32) but, until now, not further away from source.

In 2022–2023, International Ocean Discovery Program (IODP) Expedition 398 (33) drilled the marine rifts of the central South Aegean Volcanic Arc at eight sites around Santorini Volcano to depths of up to 900 m below the seafloor (Figs. 1 and 2A). Two aims were, first, to use the basin sediments as time capsules to recover a complete record of Neogene-Quaternary volcanism and, second, to seek deposits from eruptions that entered the sea as pyroclastic

currents from nearby volcanic centers. However, the presence of 200 m of KPT in the rift basins, much thicker than the 1 to 5 cm of atmospherically transported KPT coignimbrite ash previously sampled by shallow gravity coring on neighboring bathymetric highs (14), was not anticipated. The discovery highlights the importance of offshore deep drilling in increasing our understanding of large eruptions with a potentially global impact such as the KPT.

The marine rift basins containing the KPT megabed are situated 120 to 140 km west of Kos and 30 to 40 km northeast of the Christiana-Santorini Kolumbo Volcanic Field (Figs. 1 and 2A) (34, 35).

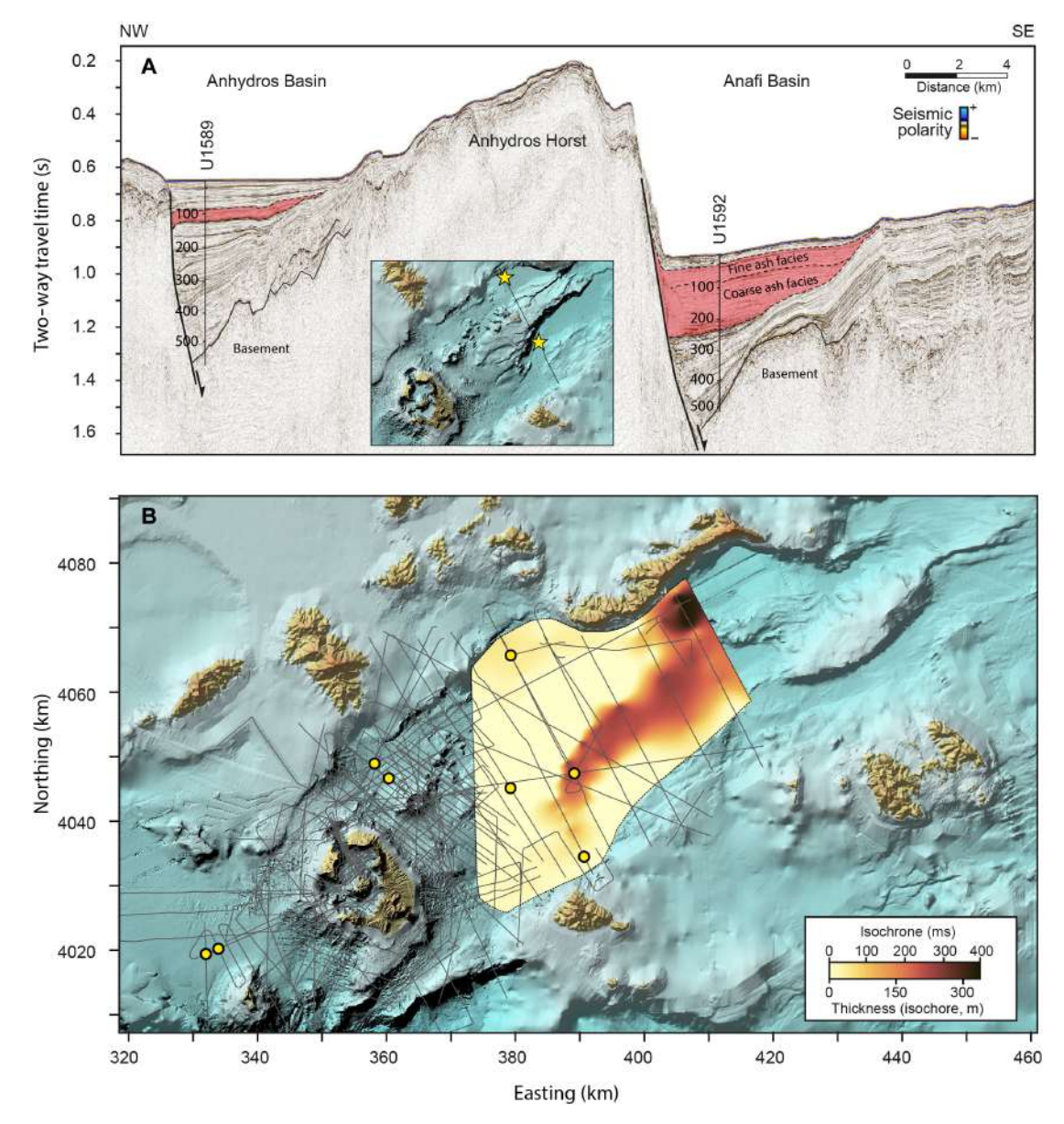


Fig. 2. Distribution and thickness of the KPT ash megabed from core-seismic integration. (A) Seismic profile across the Anhydros and Anafi Basins, showing the KPT megabed. The profiles show several seismic stratigraphic packages infilling the basins and lying on Alpine basement. Two-way seismic travel time is converted to depth (in meters below sea floor) on the drill site scale constructed by core-seismic integration using shipboard seismic velocity data. The KPT megabed is shown in pink. The dotted line separates the coarse-ash (CA) facies from the overlying fine ash (FA) facies. The basal lithic-crystal facies is too thin to be resolved. (B) Two-way travel (TWT) time isochrones for the KPT ash megabed were derived by integration of the drill core stratigraphy with seismic profiles. The TWT values were then converted to thickness using shipboard measurements of core *P*-wave velocity. The gray lines are published seismic profiles, and the yellow circles are the IODP Expedition 398 drill sites outside of Santorini caldera.

The basins lie on 20 km of rifted continental crust, with an earlier east-northeast to west-southwest Pliocene rift (the Christiana Basin) and a northeast (NE)-southwest (SW)-trending system of half-graben rifts (the Anhydros, Amorgos, and Anafi Basins) of Pleistocene age (34–36). Up to 1.4 km of volcaniclastic, tuffaceous, and nonvolcanic sediments fill these NE-SW basins above continental basement, as imaged by a dense array of over 3000 km of single and multichannel seismic profiles (34, 36). Until IODP Expedition 398, the nature of the basin fills had only been characterized by offshore seismic stratigraphy [(36) and the references therein].

Products of the Christiana-Santorini-Kolumbo Volcanic Field dominate the volcaniclastic fill components of the rifts (22). Christiana Volcano has been extinct since ~1.6 Ma (36). The earliest onland activity at Santorini dates to 0.65 Ma (37). Following the large "Archaeos" eruption in the Middle Pleistocene (22), most of Santorini's explosive eruptions took place <0.25 Myr ago and form layers in the caldera cliffs of Santorini (table S1) (37) and in the marine tephrostratigraphic record (14, 38). The last eruption of Kolumbo took place in 1650 CE (39), and the last eruption of Santorini took place in 1950 CE. In what follows, we describe the KPT megabed, a uniquely well-characterized example of distal submarine ash from a large silicic caldera-forming eruption, and we discuss its emplacement mechanism and environmental impacts.

RESULTS

The KPT ash megabed was intersected at the four drill sites shown by stars on Fig. 1, with drilling recoveries of 68 to 90% (Table 1 and fig. S1). The present-day water depths at these sites are between 326 and 693 m (legend, Fig. 1). The constituent ash of the megabed was characterized by grain size and component analysis (Figs. 3 to 5 and table S2) and was correlated between the different drill sites and onland KPT deposits by tephra stratigraphy and by chemical fingerprinting of glasses and minerals (Fig. 6 and tables S3 and S4). The megabed is thickest in the Anafi (205 m, U1592) and Anhydros (30 m, U1589) rift basins, and thinner on the margin of the Anafi Basin (8 m, U1599) and on the horst between the two basins (5 m, U1600) (Figs. 2 and 3). The age was constrained by the presence of previously dated Santorini tephras above and below the megabed (table S1). It lies stratigraphically between the Lower Pumice 2 and Cape Thera eruptions of Santorini, previously dated at 177 and 157 ka, respectively, using gravity cores of condensed sequences (table S1). This is consistent with the previously published 161 \pm 2 ka age of the KPT eruption (14, 28).

The megabed consists of unconsolidated ash, with subordinate pumice and lithic clasts of lapilli size (Fig. 4, A to E). The juvenile component is highly vesicular and includes two main varieties of pumice shards: a dominant population of tube pumices with stretched vesicles (Fig. 4F), and a secondary population of frothy pumices with larger, more equant vesicles (Fig. 4G). Pumice clasts are commonly rounded due to abrasion during transport. Glass compositions of pumices and vitric shards in both layers are identical to those of onland KPT samples and are different from glasses of Santorini and Kolumbo or of Milos Volcano to the west (Fig. 6, A to C, and table S3) (14).

Pumices from the ash megabed contain a crystal assemblage dominated by plagioclase (An_{22-23}), sanidine (Or_{72-90}), quartz, biotite, and magnetite (table S4). The plagioclase composition is similar to that in onland KPT [$An_{25\pm5}$ analyzed as part of the present study; An_{17-25} in (40)], as is the sanidine composition [Or_{-67} ; (40)]. The biotite crystals in the megabed have the same major element compositions as those of the onland KPT, which are higher in MgO and lower in FeO than biotites from the nearby rhyolitic Kolumbo Volcano (Fig. 6D).

Lithic components in the megabed include fresh or altered lava and scoria. Macroscopic bioclastic components are concentrated toward the base. They are broken, abraded, and include coral fragments, shell fragments (Bivalvia and Gastropoda), Pteropoda, Bryozoa, Arthropoda (Balanus), echinoid spines and plate fragments, and ostracods, as well as fish vertebrae. Foraminifera and nannofossils are found throughout the megabed and include reworked Pliocene and Pleistocene species. The nannofossil assemblage is characterized by the occurrence of warm-water species such as *Rhabdosphaera clavigera* and *Umbilicosphaera sibogae* that have possibly been transported from the photic zone. The foraminifer fauna are typical of Late Pleistocene Mediterranean biostratigraphic zones (41). The megabed is assigned to Zone MPle2b on the basis of the paracme top of sinistrally coiled *Neogloboquadrina* spp. (<0.51 Ma).

Assemblages of benthic foraminifera in marine sediments provide estimates of paleo water depths (42). Those immediately below the ash megabed give water paleo-depths of 750 to 1000 m and 300 to 600 m at Sites U1592 and U1589, respectively, showing that the megabed was emplaced in a shallow marine environment. An abundance of reworked species below the megabed at Sites U1599 and U1600 precludes paleo-depth estimates. The megabed can be subdivided into three lithofacies, which are described with emphasis on the thickest occurrence at Site U1592 (Fig. 3).

Lithic-crystal sand: At three sites (U1592, U1599, and U1600), the base of the megabed is a ~2-m-thick layer of lithic- and crystal-rich (LC) sand containing less than 20 wt % of pumice and less than a few wt % of fine ash but with abundant fragments of corals and shells (Fig. 5). The sand is bedded on a decimeter-scale, some of the beds being rich in pyroxene, probably entrained from underlying Santorini tuffs, and others being rich in biotite. A rip-up clast of ash is present.

Site	Water depth (mbsl)	Penetration (mbsf)	Holes with KPT	Top of KPT (mbsf)	Base of KPT (mbsf)	Thickness of KPT (m)	% Recovery o KPT interval
U1589	484	622	A, B	88	118	30	83
U1592	693	528	В	31	236	205	68
U1599	592	698	A, B	36	44	8	90
U1600	326	189	A, B	15	20	5	84

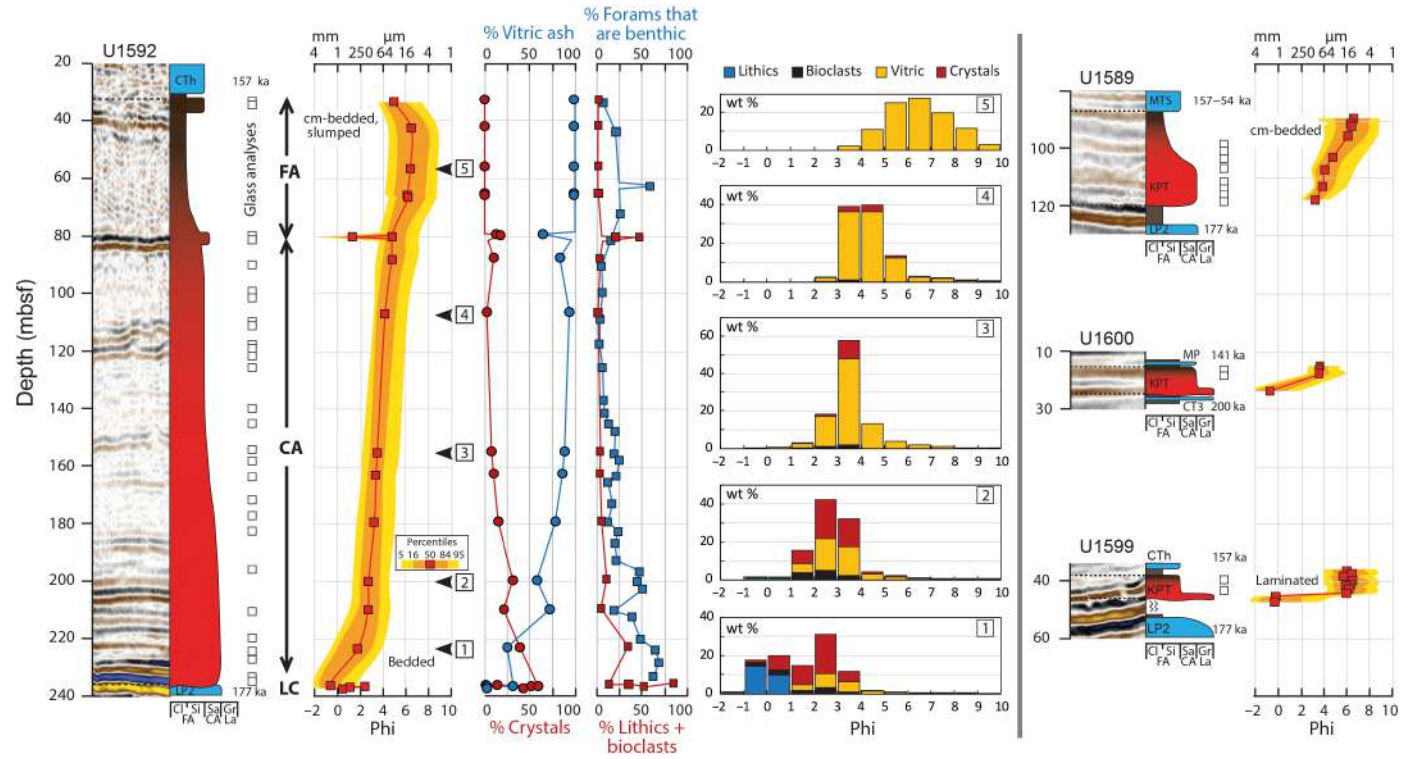


Fig. 3. Stratigraphic sections through the KPT ash megabed. The data for all four drill sites show seismic profiles, the levels of chemically analyzed glasses, and variations of key grain-size parameters (5th, 16th, 50th, 84th, and 95th percentiles) with height in the bed. At Site U1592, component abundances are also plotted with height, and grain-size histograms of five representative samples are presented. The percentages of foraminifera that are benthic species are also plotted. Granulometry abbreviations: Cl, clay; Si, silt; Sa, sand; and Gr, gravel (for nonvolcanic sediments); and FA, fine ash; CA, coarse ash; and La, Lapilli (for volcaniclastic sediments). Eruptions of Santorini: CT3, Cape Therma 3 (200 ka); LP2, Lower Pumice 2 (177 ka); MP, Middle Pumice (141 ka); MTS, Middle Tuff Sequence, a succession of eruptions from Cape Thera (157 ka) to Upper Scoria 2 (54 ka) and including MP. mbsf, meters below sea floor.

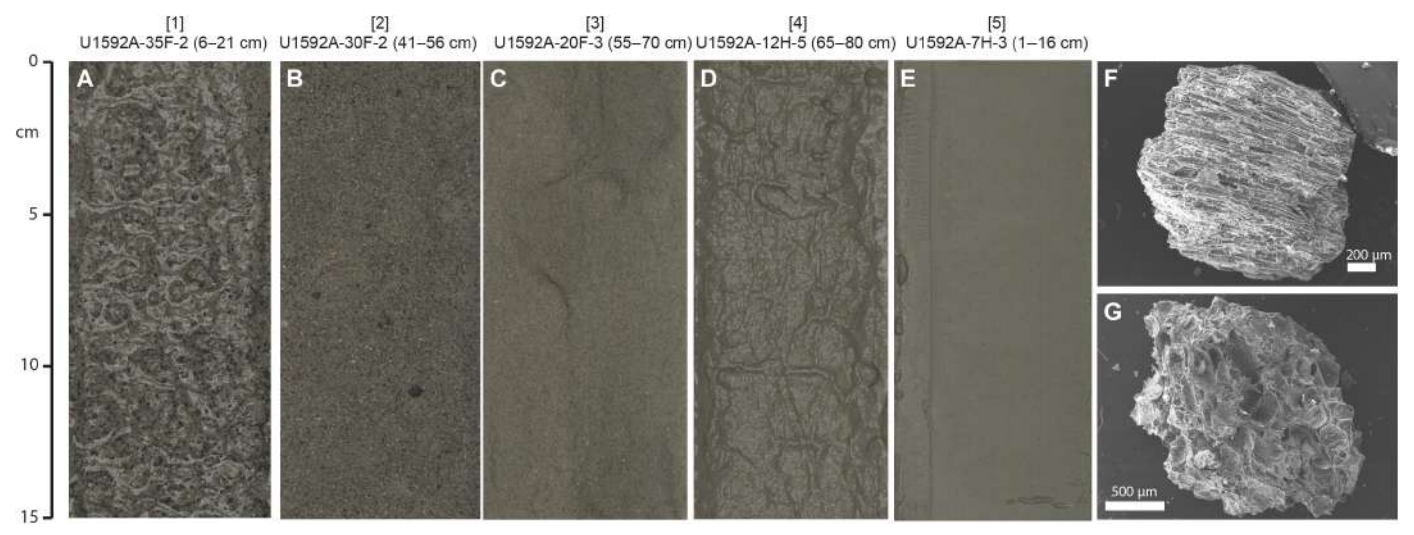


Fig. 4. Products of the KPT ash megabed at drill Site U1592. (A to E) Samples corresponding to the five grain-size histograms ([1] to [5]) in Fig. 3. In each case, the samples lack sedimentary structures. The surfaces are wet and any apparent structures are due to surface water effects. (F and G) Scanning electron microscopy images of representative ash pumice shards from Site U1592: (F) tube pumice and (G) frothy pumice [both from sample U1592A-25F-4 (50 to 56 cm)]. Sample names are read as follows: Sample U1592A-35F-2 (6 to 21 cm) was collected at 6 to 21 cm from the top of section 2 of core 35 of Hole A at drill Site U1592; the letters F and H refer to the drilling technique used.

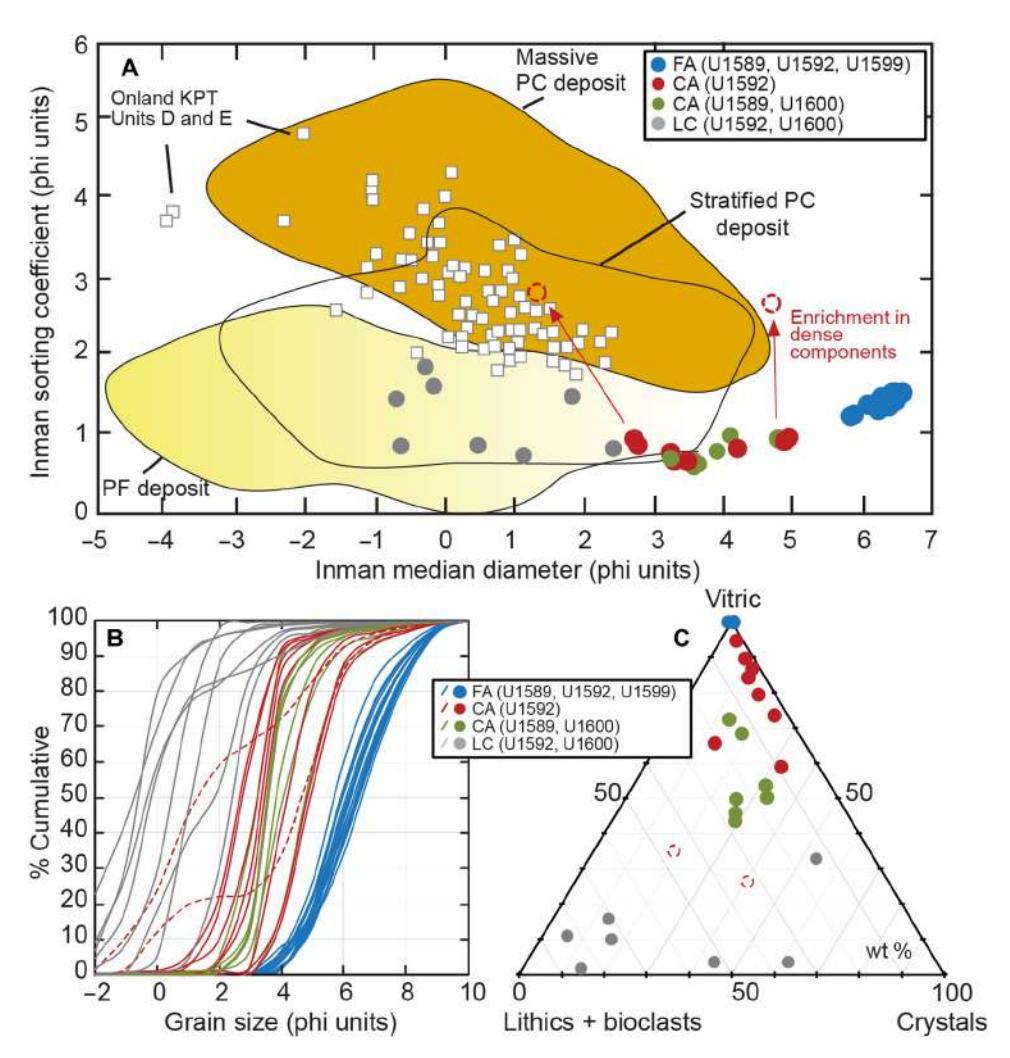


Fig. 5. Grain-size data for the KPT ash megabed. (A) Grain-size characteristics using Inman sorting and median diameter parameters (80). The median diameter is ϕ_{50} , and the sorting parameter is $(\phi_{84}$ - $\phi_{16})/2$, where the phi values are the 84th, 50th, and 16th percentiles of the grain-size distributions. Data for ignimbrite from onland eruption units D and E from (10) are also shown as squares. The data are compared to fields for the deposits of subaerial pyroclastic currents (PC) and pyroclastic falls (PF) (81). The two samples of coarse ash enriched in dense components (red, dashed) are from -80 m below sea floor at Site U1592. (B) Cumulative grain-size curves, showing a well-developed distribution grading from bottom to top. (C) Componentry of the samples from Sites U1592, U1599, and U1600. Two samples from 80 m below sea floor at Site U1592 show enrichment in lithics and bioclasts (red, dashed). LC, lithic-crystal facies; CA, coarse ash facies; FA, fine ash facies.

Coarse ash

Coarse ash: The main megabed facies is 155 m thick at Site U1592, 20 m thick at Site U1589, and a few meters thick at Site 1600. It consists of well-sorted (sorting coefficient ~1 φ) coarse ash with a median grain size in the range 2 to 4 φ (250 to 63 μm) (Figs. 3 and 5). The φ grain-size scale is defined in Materials and Methods. The ash is mostly composed of >85 wt % glass shards and crystals (mostly feldspar and biotite), but subordinate (<15 wt %) lithics and bioclasts are also present. The lithic and bioclast contents throughout the coarse ash (CA) facies at Sites U1589 and U1600 are higher than those at Site U1592. The CA facies is massive to diffusely bedded, the latter being defined by subtle fluctuations in the proportions of the different components. There are no traces of bioturbation by burrowing organisms.

The CA facies forms a single graded bed, with systematic variations of a number of parameters with height (Fig. 3).

- 1) The median grain size decreases from $0 \Leftrightarrow at$ the base to $4 \Leftrightarrow at$ the top, the grading being of distribution type (43), involving joint shifts of the median, fine tail, and coarse tail of the grain-size distribution with height (Figs. 3 and 5B).
- 2) The abundances of dense components (free crystals, lithics, and bioclasts) decrease upward.
- 3) The percentage of benthic species in the total (benthic + planktonic) foraminiferal population decreases upward, benthic species being heavier than planktonic ones (table S5).
- 4) Heavier species of planktonic foraminifera (Globoconella inflata, Truncorotalia truncatulinoides, and Truncorotalia crassaformis) decrease upward at the expense of lighter species (Turborotalita quinqueloba, Neogloboquadrina pachyderma, and Neogloboquadrina incompta).

Conversely, components that are small or light (glass shards and tests of lighter planktonic species) increase upward in the CA facies.

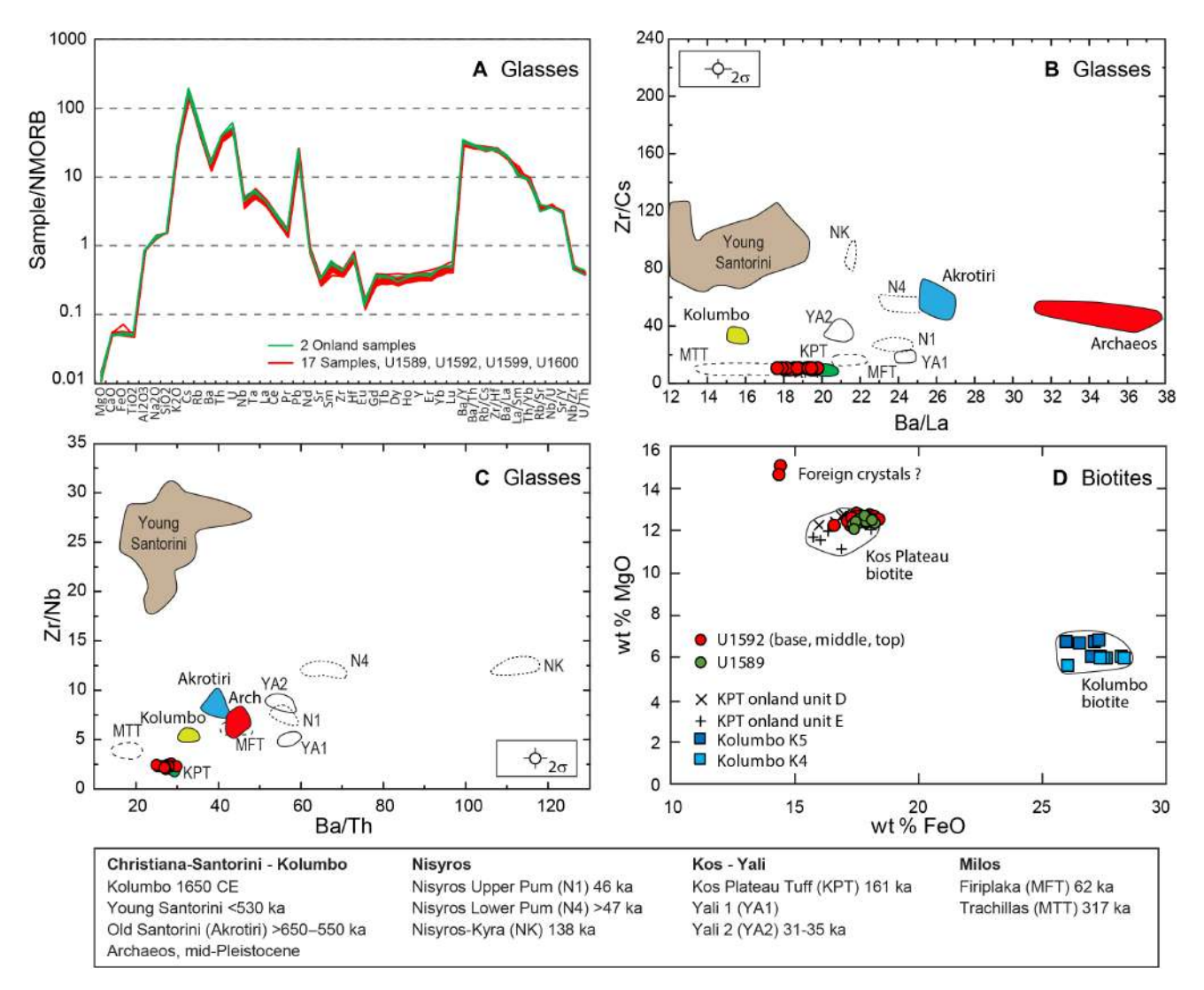


Fig. 6. Chemical data for glasses and minerals. (A) Glass element spectra normalized to N-MORB for 17 representative ash megabed samples (from the four drill sites in Fig. 1) and two onshore KPT pumice samples, showing identical compositions. (B and C) Incompatible trace element ratio plots showing the compositional similarity of onland (green area) and offshore (red dots) samples of the KPT, and the differences with other volcanic centers of the South Aegean Volcanic Arc including Santorini and Kolumbo (14, 22). Typical standard deviations on the analyses are shown. (D) Major element comparison of biotites in the offshore and onland KPT samples and with offshore samples from Kolumbo. Kolumbo unit K5 is the 1650 CE eruption and older Kolumbo unit K3/4 has an age yet to be determined.

These trends indicate extremely efficient hydraulic sorting in the submarine transport system.

Fine ash

Fine ash: This facies makes up the top 45 m of the megabed at Site U1592, the top 10 m at Site U1589, and the whole unit at Site U1599. At Site U1592, it is separated from the underlying CA facies by a ~1-m-thick level of lithic and crystal enrichment (80 m below sea floor; Fig. 3). The fine ash (FA) facies consists of well-sorted (sorting coefficient 1 to 1.5 φ), massive to bedded glassy fine ash (Fig. 4E) with a median grain size of 5 φ (32 μ m) or more (Fig. 5A) and subordinate crystal fragments, foraminiferal tests, nannofossils, and clay. The bedding is commonly disturbed, probably due to postdepositional slumping, and folds are present in the top ~5 m at Site U1592. These structures crosscut the cores and cannot be

due to core disturbance effects (44). Bioturbation structures are rare to absent; possible millimeter-wide burrows are present in the top few meters of the FA facies at Site U1592. The sparse foraminiferal population in the FA facies is dominated by low numbers of infaunal benthic foraminiferal surviving species (e.g., *Bolivina* spp., *Bulimina* spp., and *Cassidulina* ssp.) tolerant to environmental stress and/or recolonizing species. The FA facies is capped by a final 2.5 m of coarse ash.

Core-seismic integration using shipboard core acoustic velocity measurements, combined with recognition of reflections from key lithological horizons, allows us to correlate the KPT megabed across the rift basins between the four IODP drill sites using our preexisting dense array of single channel and multichannel seismic profiles (34, 36). The basal LC sands are represented by a high-amplitude reflector at the base of the megabed, which is generally conformable

on underlying strata (Fig. 2A). The CA facies appears as diffusely to well bedded on seismic profiles, probably due to fluctuations in component proportions. The internal subhorizontal reflectors interpreted as bedding are generally continuous laterally, with some lenticularity. The FA facies is seismically transparent to bedded, separated from the underlying CA facies at Site U1592 by a prominent reflector at 80 m below sea floor, which is interpreted to be the lithic/crystal-enriched layer separating the CA and FA facies at the same site (Fig. 3). The megabed can be traced across the Anafi basin, thickening from 200 m at Site U1592 northward into the southern end of the Amorgos Basin, where it reaches ~300 m in thickness (Fig. 2B) (beyond which there are no seismic profiles).

Integration of the megabed thicknesses yields a volume of 73 \pm 2 km³, about three quarters of which is the CA facies and the remaining quarter is the FA facies (Fig. 2B). Note that this is just the volume within the study area covered by our seismic profiles and that the complete extension of the megabed is unknown, especially in the Cretan Basin in the south. Shipboard measurements on the cores allow precise conversion of bulk volume to dense rock equivalent (DRE; Materials and Methods). The DRE volume is that of erupted magma and rock after removal of all pore space from vesicles and intergranular voids. The conversion factor was determined by measuring water content, bulk density, grain density, and solids density from samples recovered by coring using the shipboard moisture and density facilities. The conversion factor is 0.387 ± 0.021 (with no significant difference between the CA and FA facies), giving a DRE volume of $28 \pm 1 \text{ km}^3$. Using the componentry results (Fig. 5C), we calculate the DRE volumes of magma (glass + crystals), rock and bioclasts to be 26, 1, and 1 km³, respectively.

DISCUSSION

Correlation with the onland KPT

The similarities of glass and mineral compositions, stratigraphic position, and age of the ash megabed to those of the KPT provide a robust correlation between the two events that significantly increases the known volume of products from that eruption. Detailed correlation with specific onland eruption units has not proven possible, because glass compositions vary little between the onland KPT eruptive units, as shown by published data (45) and confirmed by additional analyses of glasses from onland units D and E that we carried out in the present study (Fig. 6 and table S3). It seems reasonable, however, to assume that the megabed derives mainly from KPT units D and E. From onland studies, these are the most voluminous units of the eruption [estimated to be ~8 and ~25 km³, respectively; (30)], and they each consist of diffusely stratified to massive ignimbrite with basal and intraformational lithic breccias indicative of emplacement by high-energy pyroclastic currents (30). With a thick and coarsegrained basal breccia, onland unit E is postulated to represent the eruption climax and onset of caldera collapse. Although the main pumice type onland is a crystal-rich tube pumice, similar to that in the ash megabed, other pumice types are also present in unit-dependent amounts (30, 46). In particular, a frothy pumice was coerupted with the tube pumice in proportions of up to 10% in units D and E, but not in units A to C (46). The KPT tube and frothy pumices may correspond to our two endmember shard types in the ash megabed (Fig. 4, F and G), supporting correlation with onland eruption units D and E.

The bulk eruption volume of the KPT products has been estimated by extrapolating onland thicknesses across an inferred areal

extension of ~8000 km², giving values in the range of 90 to 110 km³ [see (30) and the references therein]. The associated uncertainty is very large, because three quarters of that area is under the sea. Adding the 73-km³ ash megabed (and accepting that, like onland pyroclastic current deposits, this contains some entrained accidental material) increases the total area affected by the KPT pyroclastic currents (and their equivalent submarine flows) to >14,000 km², and raises the volume to 163 to 183 km³. Furthermore, adding the known 33 km³ of distal coignimbrite ash fallout (14) raises the total bulk volume for the eruption to ~210 km³ (81 km³ DRE using our IODP conversion factor of 0.387 or eruption magnitude 7.3). This is a minimum estimate because it neglects any other distal submarine ash beds around Kos.

Generation of the ash megabed

Volcaniclastic megabeds can be generated directly from explosive eruptions or by mass wasting events from volcanic islands and submarine shelves triggered by high precipitation, earthquakes, tsunamis, or long-term sea level changes (2, 20, 24). The chemical uniformity, massive to diffusely bedded nature, and well-developed vertical particle size and density grading together imply that the KPT submarine ash megabed was laid down by a single eruptive event. The absence of bioturbation, in contrast to densely burrowed background marine sediments in the Expedition 398 cores (oozes and muds), implies a rate of sediment aggradation too rapid for surface repopulation by burrowing organisms, which typically requires months to years even in less destructive modern examples of seafloor disturbance (47).

The strong rift confinement and sedimentological characteristics (graded bedding and hydraulic sorting) of the megabed show that it was emplaced mainly by submarine gravity flows. Distribution size grading is characteristic of sedimentation from turbulent suspensions with particle concentrations of less than about ~20 vol % in laboratory flume experiments (43), suggesting that the parent flows were mostly turbidity currents, although we cannot rule out involvement of debris flows or granular slurries at some levels. Particle concentrations of this magnitude are commonly estimated from in situ measurements of modern turbidity currents (48). A component from fallout through the water column (e.g., from subaerial plumes and umbrella clouds, pumice raft attrition; sea-crossing pyroclastic currents; and submarine suspension plumes) cannot be excluded. However, fallout would have produced a thinner, less channelized, deposit (2, 8, 49) with equally thick ash accumulations outside of the rift basins, and shallow gravity cores on nearby bathymetric highs yield submarine KPT ash layers only 1 to 5 cm thick interpreted as windtransported coignimbrite ash (Fig. 1) (14). The rift-confined megabed could conceivably have been fed by posteruptive resuspension of ash from the rift shoulders; however, the great thickness and systematic grading seems to preclude this as the sole mechanism (Fig. 2). The combination of great thickness, large volume, rapid emplacement as a single turbidity current event, massive to diffusely bedded nature, upward fining, and distribution grading makes the term "megaturbidite" (used hereafter) appropriate (16, 50).

We interpret the CA facies of the megaturbidite as the product of progressive aggradation from a sustained, but pulsatory, stream of ashrich turbidity currents, generated by (i) syn-eruptive entry of pyroclastic currents into the sea, followed by (ii) slumping and remobilization. The unsteadiness in sediment supply, resulting in laterally continuous internal reflections with possible upward-fining para-sequences, may have been either source derived or locally

derived due to flow divergence around bathymetric obstacles, pulses in remobilization, or intrabasinal sloshing effects (51). The LC sand at the base of the megabed is interpreted as a mixture of entrained substrate and dense components deposited at the leading edge of the turbidity current stream. The fines-depleted nature of the sand may be due to winnowing of vitric ash from the highly turbulent flow front. Although the ~1 km³ of bioclastic material in the megabed bears witness to important seafloor erosion upstream, there are no large-scale unconformities visible on seismic images within the Anafi and Anhydros Basins themselves (Fig. 2A). This shows that, by the time the currents arrived in the basins, they were incapable of scouring the substrate on a large scale, although up to a few meters of erosion is permitted by the resolution of the seismic images. Only the presence of ash rip-up clasts and an accumulation of diffractions at the base of the LC facies (Site U1592; Fig. 3) are indicative of minor scouring of the basin floors.

During sedimentation of the CA facies, large and dense components (crystals, lithics, and dense bioclasts), along with heavier foraminifer tests (benthic and heavier planktonic species), settled first, while vitric ash and lighter planktonic species were retained in suspension to fall out later as the flow waned. The upward decrease of benthic foraminifera, which mimics the upward decrease in lithics and dense bioclasts (Fig. 3), may also be, in part, attributed to smothering of the sea floor by the turbidity currents, cutting off the supply of seafloor-derived material. In the absence of any features indicative of hot deposition (sintering, gas segregation pipes, and oxidation coloration), and, given the large distance from the volcanic source, we infer that the megaturbidite in the Anafi and Anhydros Basins was emplaced cold (16, 24).

The FA facies forms a sedimentologically and seismically distinct layer above the CA facies (Figs. 2A and 3). Being composed almost entirely of massive to laminated fine vitric ash, it clearly records the end phase of megabed emplacement: the fine-grained tail of the turbidity current event (52), probably followed by prolonged ash resuspension by wave action and any slumping that may have taken place. Sedimentation of the FA facies may have occurred in a grain-by-grain Stokesian manner or by en masse collapse of suspended sediment clouds as plume instabilities (53). Apart from perhaps the top few meters, sedimentation of the FA facies took place too rapidly (months to years) for the recovery of mature benthic communities. The occurrence of slump folds in the upper FA facies implies instabilities due to seismic shaking or pore fluid overpressures following rapid sediment aggradation (2).

Published studies of the KPT eruption (10, 11, 30), of modern (18, 54) and ancient (22, 24) submarine deposits formed by the entry of pyroclastic currents into the sea, and of laboratory flume experiments (17, 19) jointly provide a basis for understanding the genesis of the ash megaturbidite. The terrestrial KPT deposits from eruption phases D and E are stratified to massive ignimbrite and lithic breccias laid down by a stream of quasi-steady pyroclastic currents that would have entered the sea at high temperatures (30). Pyroclastic currents crossing the shoreline are believed to split into two parts: a dilute upper part that travels across the sea surface and a dense lower part that plunges below it. KPT tuffs on Tilos Island and the Datça Peninsula (Fig. 1) have been interpreted as the deposits from the sea-crossing flows of the eruption (10), while a thick sediment layer visible on seismic profiles around and inside the Kos caldera has been interpreted as the proximal submarine facies (29, 31).

As the dense, lower levels of the pyroclastic currents entered the sea, they would have entrained sea water and transformed into cold, water supported gravity flows. Experiments have shown that hot pumice clasts placed in water rapidly saturate and sink because the hot gases in any interconnected pores cool and change phase, pulling in the cold water (55). Cold pumice, on the other hand, floats on water before slowly saturating and sinking on a longer timescale. We, therefore, envisage that hot pumice clasts in the KPT pyroclastic currents would have rapidly been saturated with seawater and carried away in the turbidity currents. On the other hand, cold pumice clasts (or hot pumice blocks that were too large to saturate before cooling) may have floated to form pumice rafts before later saturating and sinking. As the turbidity currents traveled from source vents situated 120 to 140 km east of the Expedition 398 drilling sites, both lithic clasts and water-saturated pumice lapilli (>2 mm) would have settled out (17, 18), progressively enriching the currents in ash (<2 mm). This is consistent with the observation that the ash megabed is systematically finer grained than onland ignimbrite units D and E of the eruption (Fig. 5A), although quench fragmentation in contact with seawater may also have played a role.

Two other features of the megaturbidite are consistent with long transport. First, it is well sorted, with values more similar to those of terrestrial fall deposits than those of pyroclastic flows (Fig. 5A). Second, the megaturbidite is enriched in vitric ash relative to the KPT magma. The KPT magma contains 25 to 30 vol % of crystals [(45, 46); vitric/crystal ratio 2.3 to 3], whereas, if averaged over the height of the U1592 section, then the mean percentage of magmatic components (glass + crystals) in the megaturbidite that are crystals is 12 vol % (vitric/crystal ratio of 7.3). Hence, the megaturbidite is the product of turbidity currents that are enriched in vitric ash relative to the original magma, having lost material relatively rich in crystals upstream of the drill sites.

The separation of particles of different sizes and densities may have occurred progressively during transport of the turbidity currents. Water is known to sort particles according to their size and density more effectively than gas (2, 39). However, an additional, even dominant, mechanism may have involved violent explosions and boiling at the shoreline when the hot pyroclastic material met water (17, 18). Littoral explosions were observed at Montserrat when pyroclastic currents entered the sea (54); the explosions are believed to have sorted the pyroclastic material, depositing the coarse (lithics, large bioclasts, and water-saturated pumices) and dense (lithics and crystals) particles near the shoreline and generating ash-rich turbidity currents that then traveled into deeper water. Laboratory flume experiments running hot ash into water also generate vigorous mixing zones in which ash is separated from coarser fractions (17, 19). This raises the possibility (testable by future drilling) that the ashrich KPT turbidity currents were generated close to the shoreline around the ancient Kos Volcano. Last, settling of ash from sea-crossing pyroclastic currents, which are believed to have traveled up to ~60 km from source (10, 11), may also have contributed to the submarine turbidity currents.

Delivery of the ash-enriched turbidity currents to the basin sites

We infer from our data that the KPT turbidity currents flowed west-ward 120 to 140 km parallel to the volcanic arc until they were trapped in the Anafi, Anhydros, and Amorgos rift basins (Fig. 1). Most of the flow route would have been under water, as eustatic sea level 161 kyr

ago was only ~80 m below that of the present day (Fig. 1) (56). The Anafi and Amorgos Basins must have been deep troughs at that time to have "instantaneously" accommodated the KPT ash, since subsidence of 200 to 300 m could not have occurred within the duration of the eruption. The deep basins and the high master-fault scarps defining their western boundaries thereby served as bathymetric traps for the turbidity currents, allowing great thicknesses of ash to accumulate. Upon reaching the Anafi and Amorgos Basins, the turbidity current suspensions either had sufficient inertia or had inflated sufficiently to overspill the ~400-m-high Anhydros Horst and to deposit 5 m of ash at Site U1600 and 30 m at Site U1589. The higher lithic and bioclast contents of the CA facies at Sites U1600 and U1589 compared to those at Site U1592 (Fig. 5C) may be due to entrainment of debris from the horst during overspilling. Two endmember scenarios can be envisaged to generate the thick basin fills: (i) turbidity currents of low concentration maintained for a long time or (ii) turbidity currents of higher concentration maintained for a shorter time.

To test whether the seafloor bathymetry would have directed the KPT currents to the basins NE of Santorini, we used idealized models of currents with constant excess density (equivalent to assuming that the particulate load was fully suspended) that neither erode or deposit sediment nor entrain ambient ocean water. The currents were discharged for 24 hours across a digital elevation model of the seafloor bathymetry, sourced from the circumference of a 30-kmradius cylindrical volume around the Kos Volcano. The transformation from gas-supported pyroclastic currents to water-supported turbidity currents was assumed to have taken place entirely within the source cylinder. The supply (i.e., eruption) rate was chosen to be appropriate for the KPT eruption by assuming that the excess density of the flow was due to suspended ash. Given the simplicity of the models, which lack many features of real-world turbidity currents [suspended particles, vertical stratification, mass loss through sedimentation, mass gain through seafloor erosion, and entrainment of ambient seawater; (57–59)], the calculations serve simply to trace possible pathways of the KPT submarine flows governed by the complex seafloor bathymetry. They are unable to realistically simulate realistic flow-front velocities, emplacement timescales, or depositional maps. The Hunga Tonga eruption-fed turbidity currents have also been modeled using a constant-density flow model, and a reasonable correspondence between model flow pathways and real flow paths was found (4).

The equations, parameters, and assumptions of the models are discussed fully in Materials and Methods. A representative model is shown in Fig. 7, and others with different parameters are presented in fig. S2. In all of the models, the highly unsteady current front is followed by a quasi-steady body that is maintained over many hours. Flow streamlines in the current body imaged by tracers released 6 and 12 hours after the supply onset are directed by the bathymetry to the east, south, and west of the Kos Volcano (a landmass existed to the north 161 ka when sea level was 80 m lower than today). To the west, the currents are directed down very gentle (average ~0.2°) bathymetric gradients into the Anafi and Amorgos Basins, from which (as the currents accumulate in those basins) they spill over into the Anhydros Basin. Although these simple models do not capture the full, highly complex real-world physics of the KPT turbidity currents, they show that the westward flow trajectory from Kos to the rift basins NE of Santorini inferred from our field study is feasible and open the way for more complete modeling of long-distance runout [e.g., (59)].

The KPT example in the spectrum of volcanogenic turbidity currents

Submarine megabeds result from catastrophic re-sedimentation events such as earthquakes, tsunamis, slope failures, or volcanic eruptions (60, 61). Although the volumes of transported sediment can be very large [up to 10^2 to 10^3 km³; (48)], most megabeds are less than a few tens of meters thick, making the KPT one of the thickest Quaternary examples known. The KPT megabed is much thicker than the ash turbidites generated at comparable (~100 km) distances from the volcanic eruptions at Hunga-Tonga in 2022 [<50 cm at 100 km; (23)] and Montserrat in 2003 [few centimeters at 100 km; (18)]. Moreover, the KPT eruption discharged 30 or more times more material into the sea than Hunga-Tonga (6 km³) and a thousand or more times more than Montserrat (0.2 km³). Other examples of historical shoreline-crossing pyroclastic currents such as Vesuvius (79 CE), Tambora (1815), and Krakatau (1883) are also smaller than the KPT (24). However, eruptions of similar magnitude ($M \sim 7.3$) to the KPT occur once every 10³ years globally (27), and submarine megabeds up to 150 m thick from large-magnitude eruptions at Campi Flegrei (61), Kikai (62), and Santorini (22, 63) calderas have been identified. Ancient analogs of the KPT megaturbidite are also known from the geological record (table S6), although none of these are thicker than 150 m. Examples include the Merrions Tuff (Australia), the Dali Ash (Greece), the Myazawa Tuff (Japan), and the Stanley Tuffs (USA), which are interpreted as ash-dominated, graded megaturbidites from subaerial or shallow marine explosive eruptions [(24, 25); additional references in table S6]. Like the KPT megabed, some also consist of two distinct layers: a thicker massive ash or lapilli-ash layer from the turbidity current body overlain by a finer-grained layer from the current wake or late-stage suspension fallout. Among these volcanic examples, the KPT submarine ash megabed is unique in its great thickness and in its unambiguous connection to a well-documented onland Quaternary eruption.

While emphasis is commonly placed on the onland and atmospheric impacts of large explosive eruptions, the present study serves to illustrate the huge but largely invisible effects of large volcanogenic gravity flows on the submarine realm. Infilling of the Anafi and Amorgos Basins with 200 to 300 m of ash records the ability of such low-frequency but high-impact events to resculpt the seafloor landscape over huge areas in a similar manner to large submarine landslides and their associated turbidity currents (64). Although some large, nonvolcanic turbidites have volumes comparable to or larger than the KPT submarine megabed (48), the key factor in permitting the accumulation of the KPT ash to such great thicknesses was the presence of sediment-starved rift basins that served as traps for the eruption-fed turbidity currents. This highlights the very important role of seafloor bathymetry and spatially limited depocenters in governing the thickness of gravity-flow deposits in ancient successions.

The presence of more than 1 km³ of bioclastic debris in the KPT megabed is consistent with the known ability of turbidity currents to destroy marine ecosystems and to bulk during transport due to erosion of the sea bed (4, 65). However, the amount of lithics and bioclasts accounts on average for only ~8 wt % of the entire megabed section at Site U1592, and many of the lithics may be source derived. Moreover, the vitric components are compositionally very homogeneous and, hence, mostly juvenile. The percentage of entrained material in the KPT submarine megabed is, therefore, small compared to that (about one-third) in the Hunga-Tonga submarine flows (4).

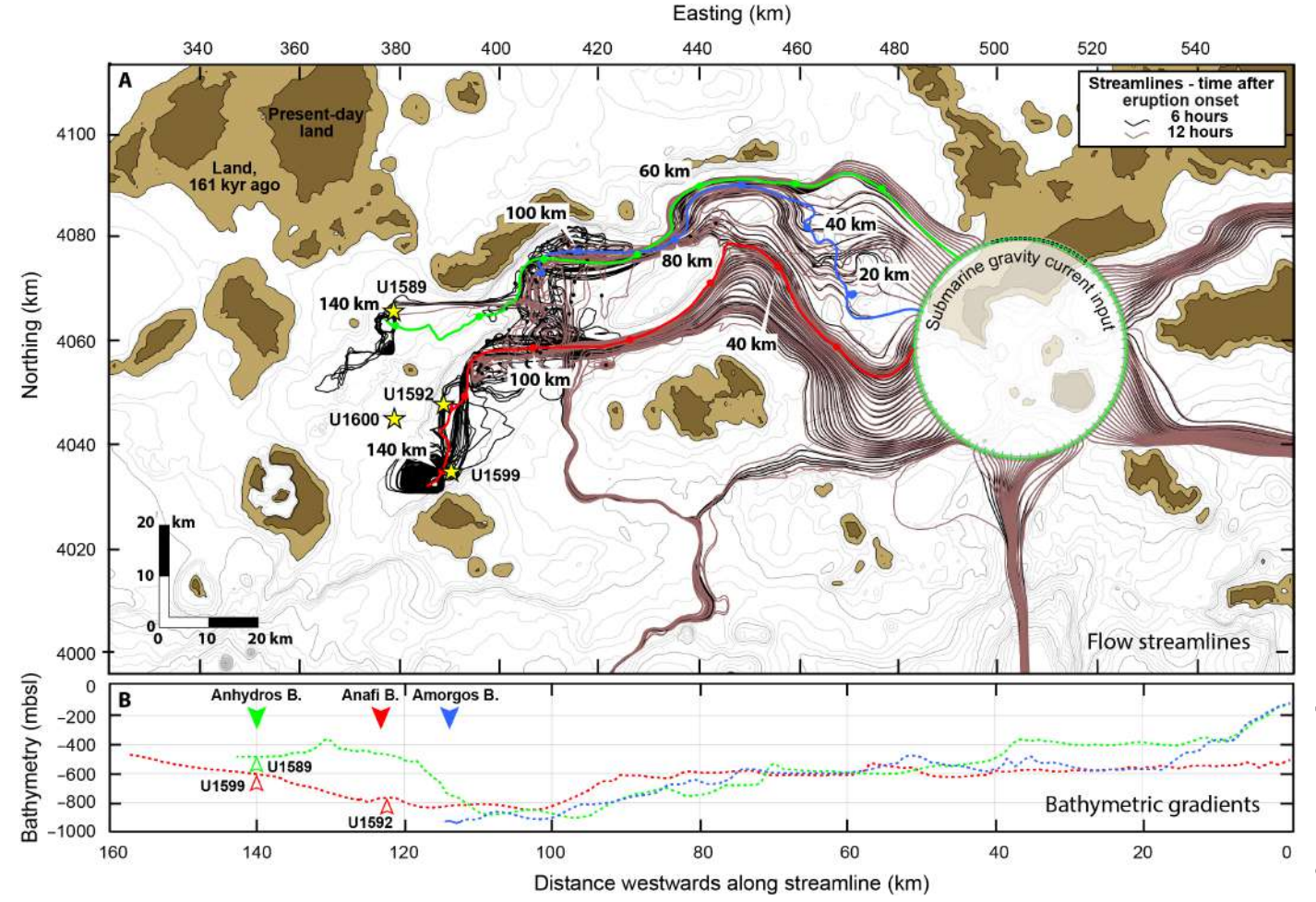


Fig. 7. Density current model showing that the KPT turbidity currents could have been directed by the regional seafloor bathymetry to the rift basins NE of Santorini. The current has a constant density and flows downslope without stopping. No particle sedimentation or basal erosion is taken into account. In this example, the flow density is 1094 kg m^{-3} (equivalent to a concentration of virtual suspended ash of about 5 vol %). The current is released from a 30-km-diameter cylindrical source volume around the Kos caldera (green circle) at a rate equivalent to a magma (i.e., virtual suspended solids) flux of $3 \times 10^9 \text{ kg s}^{-1}$, consistent with a time-averaged discharge rate smaller than the peak value for the KPT eruption $[4 \times 10^9 \text{ to } 8 \times 10^9 \text{ kg s}^{-1}; (11)]$. The supply (i.e., "eruption") is maintained for 24 hours. The current initially has a velocity of 0 m s^{-1} but then rapidly accelerates due to the bathymetric gradient. See Materials and Methods for full details. (A) Flow streamlines in the current body (well behind the transient head) visualized by neutrally buoyant tracers released 6 (black) and 12 (brown) hours after the eruption onset. Dark brown areas are present-day land and pale brown is area above the -80 -m contour, representing approximate sea level 161 kyr ago. The four deep-drilling sites concerned here are shown as yellow stars. (B) Bathymetric profiles down the three (red, green, and blue) streamlines.

It is highest (30 to 80 wt %) in the basal 20 m of the megabed at Site U1592, but less than a few wt % in the overlying 190 m (apart from some thin lithic-rich levels) (Fig. 3). While the front of the current was highly erosive, the current body, eruption fed for many hours to days (30), traveled mostly across its own deposit. Hence, while episodic reentrainment of the deposit was highly likely, most of the turbidity current was isolated from the preeruptive sea floor.

Submarine ash dispersal from pyroclastic currents

The processes by which pyroclastic currents generate atmospheric coignimbrite plumes are well understood (Fig. 8) (13). The KPT ash fall layer, ~33 km³ in bulk volume, occurs in marine sediments across the eastern Mediterranean and is thought to be mainly coignimbrite in origin (Fig. 1) (14). Coignimbrite ashes are typically fine-grained, with mean sizes of \geq 4 φ [\geq 63 μ m; (13)]. The KPT megaturbidite

highlights another mechanism for distributing large volumes of ash from explosive eruptions in marine settings. In this case, interaction of the hot dense pyroclastic currents with the sea caused efficient hydraulic sorting of particles of different sizes and densities, and the resulting ash-rich turbidity currents traveled far from the source. This is because, unless the current enters the deep-sea realm where the water is colder and saltier (66), shallow marine turbidity currents will not undergo buoyancy reversal, and the ash will be transported until the current velocity wanes or the flow encounters a bathymetric trap. In the case of the KPT, the top 45 m of the deposit in the Anafi Basin (FA facies), corresponding to ~18 km³ of ash, has similar grain-size characteristics to terrestrial coignimbrite ash. Hence, the volume of fine ash contained within just the Anafi and Anhydros Basins is comparable to that lofted by the atmospheric Phoenix cloud of the eruption.

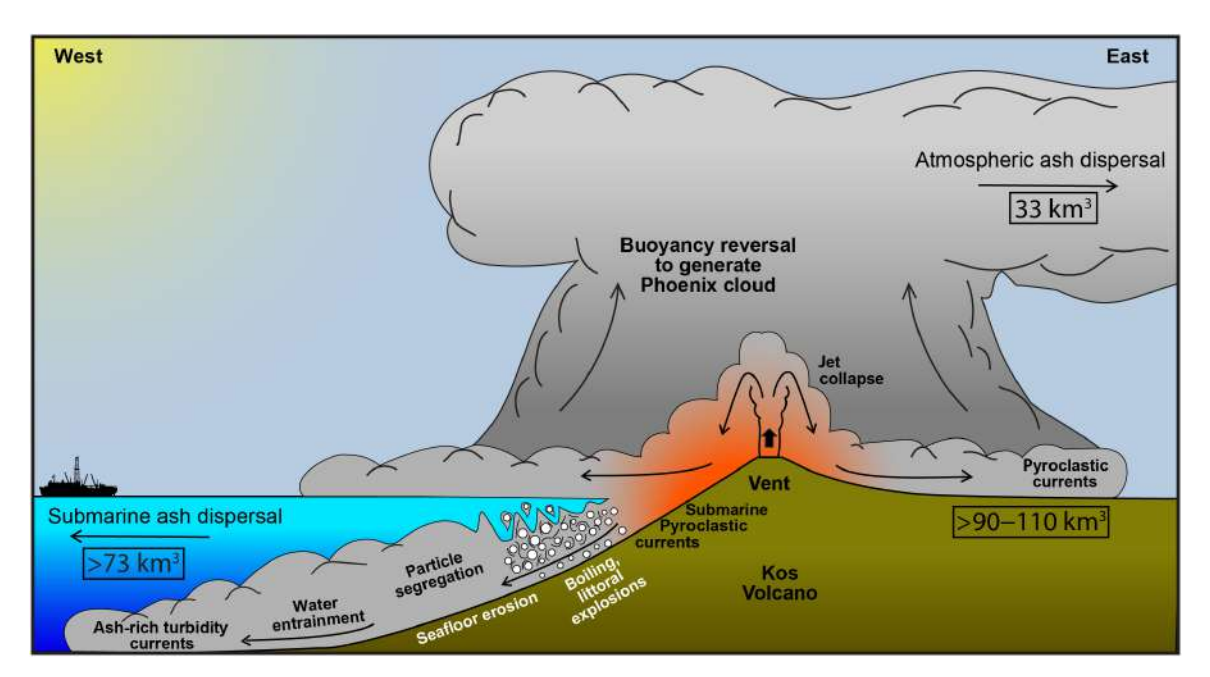


Fig. 8. Two mechanisms for the dispersal of volcanic ash from the KPT explosive eruption. The mechanism by which subaerial pyroclastic currents loft to generate atmospheric coignimbrite Phoenix plumes that are then dispersed by the wind (right) is well understood (13). However, the present paper shows that efficient particle segregation in submarine pyroclastic currents and the turbidity currents into which they transform (left) can also result in thick beds of distal ash of volume comparable to or greater than those of Phoenix plumes. The figure is not to true scale. The volume figures refer to the KPT eruption. They are bulk values (i.e., non-DRE), minimum estimates acknowledging that larger reserves of submarine eruptive products from the eruption probably remain to be discovered.

Despite the presence of 200 to 300 m of submarine KPT ash in the Anafi and Amorgos Basins, no trace of KPT deposits have, to our knowledge, survived erosion on Santorini or neighboring islands. Without IODP Expedition 398, the true extent of the KPT would, therefore, have remained unknown, highlighting the important contribution the submarine realm makes to our understanding of island volcanoes. The discovery changes our perspective of the potentially large, hidden volumes of island arc eruptions and the ability of turbidity currents to disperse fine ash far from the eruption source. The large volume and great extent of KPT ash suggest that the volumes of some explosive eruptions from island volcanoes may have been underestimated.

MATERIALS AND METHODS

IODP Expedition 398 deep-sea drilling

IODP Expedition 398 took place on the *R/V JOIDES* Resolution over 2 months, from 11 December 2022 to 10 February 2023, and drilled at 12 sites in and around the Christiana-Santorini-Kolumbo Volcanic Field (33). Details of the four sites at which the KPT megabed was recovered are given in Table 1. Two to three holes (A, B, and C) were drilled ~50 m apart at each site, and the ash megabed was intersected in one or more of these holes using either Advanced Piston Coring (9.5-m stroke) or Half-Length Advanced Piston Coring (4.7-m stroke). The core diameters were 6.2 cm. The standard array of shipboard physical property measurements was made on the cores (https://iodp.tamu.edu/labs/index.html). The cores were logged and described, taking into account artefacts of drilling and core recovery such as sediment mixing, shear-induced uparching, brecciation, biscuiting, and ash liquefaction (44). Samples of pumice lapilli and ash were

collected from the cores for chemical and mineralogical analysis. Bulk sediment samples were taken from the core catcher of every core for micropalaeontological analysis and determination of paleowater depths.

Digital elevation model

The digital elevation model (Fig. 1) was produced by merging satellite-derived Advanced Spaceborne Thermal Emission and Reflection Radiometer (ASTER) data, a community-sourced elevation model from the European Marine Observation and Data Network (EMODnet), data acquired on board the R/V Aegaeo during the Geospatial Warning Systems (GEOWARN) project, and data from the R/V Marcus G. Langseth during the Plumbing Reservoirs of the Earth Under Santorini (PROTEUS) seismic tomography project (35, 67). The swath dataset (lateral resolution of 20 m) in the area between Kos, Nisyros, and Tilos islands was obtained from three multibeam bathymetric surveys carried out on R/V Aegaeo during 2000. During the first mission, the area of Nisyros Island and the surrounding small islets were mapped using the SEABEAM 1180 (180 kHz) system, which is suitable for seabed mapping in shallow-middle depths (<500 m). The other two missions completed the mapping of the whole area of Kos-Nisyros-Tilos using the SEABEAM 2120 (20 kHz) system, which is suitable for seabed mapping in depths >500 m. By operating the systems for a total period of 12 days with an average speed of 10 knots, 3500 km² were covered from very shallow depths to depths of 2200 m. Bathymetric data in the Santorini-Anafi-Amorgos region were acquired onboard the R/V Marcus G. Langseth using the Simrad Kongsberg EM122 12-kHz multibeam echo sounder (35). Data were processed using the MB-SYSTEM open-source software (www.mbari.org/ mb-system) and merged with preexisting data (67).

Chemical compositions of glasses and minerals

Glass shards from the submarine KPT ash megabed were analyzed at 31 levels at Site U1592, 8 at U1589, 2 at U1599, and 5 at U1600. Glasses from representative pumice lapilli taken from eruptive units D and E of the onland KPT (28) and provided by O. Bachmann were also analyzed for comparison. In each case, a 63- to 250-µm glass fraction was embedded with epoxy resin into 12 predrilled holes in acrylic mounts and polishing to facilitate measurements with the electron microprobe (EMP) and the laser ablation inductively coupled plasma mass spectrometer (LA-ICP-MS). Biotite and plagioclase were also separated from samples from Sites U1592 and U1589 and from the onland KPT and were mounted in epoxy for analysis.

Major and minor elements of glasses were analyzed at two laboratories: the Laboratory of Magmatism and Volcanism in Clermont-Ferrand, France (LMV), and the GEOMAR Helmholtz Centre for Ocean Research, Kiel. Major and minor elements of crystals were analyzed at the LMV. Analyses were carried out at the LMV using a CAMECA SX-100 EMP and at GEOMAR using a JEOL JXA 8200 wavelength dispersive EMP. In both cases, an accelerating voltage of 15 kV, a beam current of 6 nA, and a 10-µm-diameter electron beam to minimize sodium loss were used. Oxide concentrations were determined using the ZAF correction method. Accuracy was monitored by two measurements each on Lipari obsidian and Smithsonian basaltic standard VGA99 (68) after every 20 analyses. All analyses with totals of >90 wt % were renormalized to 100% to eliminate the effects of variable postdepositional hydration and minor deviations in focusing of the electron beam.

Trace element contents of glass shards were analyzed by LA-ICP-MS in two laboratories: the LMV and the Academia Sinica in Taipei, Taiwan. Both laboratories used 193-nm excimer lasers with 24- to 30-µm beam sizes connected to Agilent 7500 or 7900 ICP-MS instruments. Background was counted for between 20 and 45 s, and samples for between 75 and 100 s. The internal standard was ⁴³Ca (Taiwan) or ⁴⁴Ca (LMV), with CaO contents determined by EMP on the same glass shard. The external standard was National Institute of Technology (NIST) 612, and the secondary standard was Columbia River Basalt (BCR). The GLITTER software was used to reduce the data and calibrate with standards to obtain trace element concentrations. The limit of detection was <100 parts per billion (ppb) for most trace elements and ~10 ppb for rare earth elements. The analytical precision was better than 10% for most trace elements and the analyses; the results from both laboratories were found to be the same within analytical uncertainty.

Grain-size and component analyses

Grain-size analyses were carried out on 43 bulk samples (mostly, 30 to 80 g) covering the range of lithologies. The 34 samples containing size fractions larger than 63 μ m were first sieved by hand at one-phi intervals from -2 to 4 φ . The standard phi scale of grain size is defined by $d=2^{-\varphi}$, where d is grain diameter in millimeters. Sub-63- μ m fractions from all the samples were analyzed by laser diffraction using a Malvern Mastersizer 3000 at the Institut de Chimie de Clermont-Ferrand, France, using Mie theory with an absorption coefficient of 0.001 and a refractive index of 1.56. All measurements were performed in water under ultrasonic assistance with a few drops of surfactant.

Component proportions were measured by point counting up to 400 grains under a binocular microscope (250 μ m and above) or under a polarizing microscope (125 and 63 μ m). Observation under crossed polars allowed distinction between crystals, foraminifera,

and glass in the finest size fractions. Component proportions in fractions smaller than 63 µm were assumed to be the same as in the 63-µm fraction. Component number percentages were converted to weight percentages assuming densities of 2500 kg m $^{-3}$ for lithics, 1000 kg m $^{-3}$ for bioclasts, and 2746 kg m $^{-3}$ for crystals (90% of light crystals at 2681 kg m $^{-3}$ and 10% of dark crystals at 3330 kg m $^{-3}$) (46). Densities of vitric components were taken as 800 kg m $^{-3}$ at -2 φ (46), 2300 kg m $^{-3}$ at >3 φ , and extrapolated linearly between -2 and 3 φ (69). For conversion of weight percentages to DRE volume percentages, a void-free solid density of 2680 kg m $^{-3}$ was used (see below).

Seismic data

The seismic profile shown in Fig. 2A was collected during cruise POS338 with *R/V Poseidon* in 2006 (70). A GI-pulser was used and operated in true GI mode with a primary (Generator) volume of 45 inches³ (737 cm³) and a secondary (Injector) volume of 105 inches³ (1721 cm³). Using a 600-m analog streamer with 24 channels, we defined a common midpoint (CMP) spacing of 12.5 m. Processing of these data comprised trace-editing, simple frequency filtering (10 to 500 Hz), suppression of a receiver-ghost signal by predictive deconvolution, surface-related multiple elimination (SRME), as well as spherical divergence correction, prestack time migration followed by top muting and white-noise removal. These data have a main frequency of 60 Hz, indicating a vertical resolution of 8 to 15 m.

For the mapping of the KPT (Fig. 2B), the seismic data from cruise POS338 and two other cruises between 2006 and 2019 were used (71). Single-channel seismic data were acquired in 2006 during the THERA project on R/V Aegaeo. A G-pulser was used as the seismic source, with a volume of 10 inches³ (164 cm³). The general processing comprised simple band-pass filtering (15 to 500 Hz), despiking, predictive deconvolution for the suppression of a strong bubble signal, and spherical divergence correction. To migrate the data, we binned the shot points into a regular spacing of 10 m. After migration, we applied a top-mute and white-noise removal. The vertical resolution of these data can be approximated to 8 to 15 m (using the $\lambda/4$ - or $\lambda/2$ -approximation).

During the most recent cruise POS538 with *R/V Poseidon* in 2019, we acquired seismic data with a much higher lateral resolution (CMP spacing of ~1.56 m). As a seismic source, we used a GI-pulser that was operated in harmonic mode with primary and secondary volumes of 45 inches³ (737 cm³). Seismic energy was recorded by multiple concatenated Geometrics GeoEel streamer segments, resulting in active streamer sections ranging from 190 to 250 m in length. Processing comprised trace editing, simple frequency filtering (15 to 1500 Hz), and multiple suppression by means of SRME. This was followed by spherical divergence correction, time-variant frequency filtering, prestack time migration, top muting, and whitenoise removal. With a main frequency of 125 Hz, the vertical resolution is 4 to 8 m.

All processed seismic profiles were combined into an interpretation project using KingdomSuite software. Here, we established the stratigraphic framework [following published (36) nomenclature in in all basins, except for the Anhydros Basin, for which we refined the seismostratigraphy based on new biostratigraphic age markers], mapped seismic units, and created isochron maps (vertical thickness in two-way travel time) by interpolating between the seismic profiles.

P-wave velocity, core-seismic integration, and deposit volume estimation

Integration of core data with seismic profiles requires shipboard measurement of compressional wave (*P*-wave) velocity. This was measured in situ on wet samples from the working half of split cores using the *P*-wave gantry system on the JOIDES Resolution. Measurements were conducted perpendicular to the core using caliper transducers for every section unless core quality was compromised. For more efficient contact, deionized water was applied on the lower transducer in contact with the core liner. To protect the upper caliper transducer from dirt and damage, a piece of plastic film was placed on the split core surface.

The system uses Panametrics-NDT Microscan delay line transducers, with a frequency of 500 kHz. The distance between the two transducers was measured with a built-in linear variable differential transformer. The *P*-wave passing through the sample was recorded, and first arrivals were picked as the initial rise of the first peak using an automated procedure. Velocities were manually picked only in circumstances where the automated thresholds did not align with the observed first arrival. The velocity measurement includes a correction for the core liner of known thickness.

A total of 264 discrete P-wave velocity measurements of the KPT were made at Sites U1589A and U1592A. We neglected all data when the sample description included "soupy material plunger used to compact sections." The mean velocity is 1587 m s⁻¹ with a standard error of 3 m s⁻¹ and a standard deviation of 40 m s⁻¹. We used this velocity to convert the isochron maps to isochore maps (Fig. 2B) in meters and to estimate the bulk volume of the KPT ash megabed.

Conversion of volume to DRE

The Dense Rock Equivalent (DRE) conversion factor is the volume of erupted magma and rock compared to the deposit volume after removing all pore space from vesicles and intergranular voids. The conversion factor was determined by measuring water content, bulk density, grain density, and solid density from samples recovered by coring using the moisture and density facilities on the JOIDES Resolution.

A dual-balance system was used to measure both wet and dry masses. The two coupled analytical balances, Mettler-Toledo XS204, were used to compensate for the ship motion: one acting as a reference and the other for measurement of the unknown. Before weighing sample-standard pairs, the balances were "tared" to zero based on the mean of 300 measurements; this procedure was performed every 6 hours. Standard weights of similar value to the sample's weight were placed on the reference balance, and the sample was placed on the balance for the unknown mass. Each reported sample mass is the mean of 300 measurements. If the reference and sample masses differed by more than 2 g, the measurement was aborted and then repeated after adjusting the weights on the reference balance. Typically, samples were 10 to 20 g when wet.

Immediately after samples were collected, the wet sample mass was measured. Dry sample mass and volume were measured after drying the samples in a convection oven for 24 hours at a temperature of $105^{\circ} \pm 5^{\circ}$ C and then cooling them within a desiccator for 3 hours. Dry volume was measured using a shipboard helium-displacement pycnometer with a nominal precision of ± 0.04 cm³. Each volume value consists of an average of three measurements.

For calculation of sediment bulk density, dry density, grain density, porosity, and void ratio, the traditional ODP method was used

(33), assuming a porewater salinity of 0.035 per mil and density of 1024 kg m⁻³. Because there are isolated vesicles entirely encased by glass in the pumice clasts, the measured grain density ($2473 \pm 77 \text{ kg m}^{-3}$) can be lower than the density of solids. To account for isolated vesicles, we used the highest measured grain density as an estimate of the solid density (2680 kg m^{-3}).

A total of 71 moisture and density samples of the KPT were measured on the CA and FA facies from Site U1592A and Site U1589A. The mean DRE conversion factor is 0.387 with a standard error of 0.021, slightly higher than that for the Archaeos Tuff [0.341 \pm 0.009; (22)], and no statistically significant difference between the two facies.

Microfossil assemblages and paleobathymetry

Foraminifera and calcareous nannofossils were obtained from 5- to 10-cm whole round sediment samples; most of the samples were taken from core catchers or the bases of cores, but, where appropriate, additional split-core samples were taken to better define biostratigraphic datums.

Samples were prepared by manually breaking the core into small pieces and soaking in hot water when clay was present. After 5 to 10 min, samples were disaggregated and washed over a 63-µm mesh sieve to remove all mud, silt, and ash. The washed microfossil residue retained on the sieve was dried on filter paper in low temperature at ~50°C in a thermostatically controlled drying cabinet and subdivided with a microsplitter into equal aliquots for examination of planktonic and benthic foraminifera. As a precaution against cross contamination, sieves were cleaned with jetted water, placed in an ultrasonic bath for several minutes, dried with compressed air, and thoroughly inspected between samples. For calcareous nannofossil analyses, standard smear slide methods were used for all samples using optical adhesive as a mounting medium. The nannofossils were examined under a polarizing light microscope at ×1250 magnification and were classified taxonomically (72, 73).

The taxonomy for planktonic foraminifera follows a modified version of the phylogenetic classification (74), with additional species concepts (75). The 2020 Geologic Time Scale (76) was used and updated with regional biostratigraphic schemes and datums (41, 72). Benthic foraminifer assemblages in the >125-µm grain-size fraction were the primary tool used for estimating palaeowater depths, using published taxonomies (77). Palaeowater depth ranges were estimated using the deepest calibrated depth marker contained in each sample [(42) and the references therein]. The species used (with palaeodepth ranges in brackets) are Articulina tubulosa (>1000 m), Cibicides pachyderma (200 to 700 m), Cibicidoides mundulus (>1000 m), Cibicidoides wuellerstorfi (>1000 m), Gyroidina soldanii (200 to 700 m), Hoeglundina elegans (50 to >700 m), Hyalinea balthica (200 to 700 m), Karreriella bradyi (200 to 700 m), Oridorsalis umbonatus (500 to >1000 m), Planulina ariminensis (>50 to 700 m), Trifarina angulosa (50 to 700 m), Trifarina bradyi (200 to 700 m), and Uvigerina peregrina (>100 to 700 m). The complex sedimentary and volcanotectonic settings sampled during IODP Expedition 398 resulted in some uncertainties in paleowater depth reconstructions through sediment remobilization and downslope displacement of shallow-water species.

Tephrostratigraphic age constraints

The age of the KPT ash megabed is constrained by the ages of Santoriniderived tephra immediately below and above the bed (table S1).

Flow modeling

We carried out the density current modeling using the numerical code VolcFlow, which is a freely available code that solves the depthaveraged equations of mass and momentum conservation for fluids of different rheologies over three-dimensional terrain (78). In the present application, the flows were assumed to be fully turbulent and to have a constant density in excess of that of the ambient seawater (equivalent to a saline flow or a turbidity current containing perfectly suspended particles). Several important features of real-world turbidity currents, including particle sedimentation, basal erosion, flow stratification, and entrainment of ambient seawater (57–59, 65), were neglected, as discussed below. The turbidity current was, therefore, approximated by a quasi-steady seafloor-hugging flow of constant density. The aim of the modeling was simply to test whether the seafloor bathymetry could have directed the KPT turbidity currents westward toward the Anafi, Amorgos, and Anhydros Basins NE of Santorini. The models are not presented as robust simulations of the natural submarine flows and should not be taken as such.

The governing depth-averaged flow equations are based on mass conservation

$$\frac{\partial h}{\partial t} + \frac{\partial}{\partial x} (h \nu_x) + \frac{\partial}{\partial y} (h \nu_y) = 0 \tag{1}$$

and conservation of momentum in the x and y directions

$$\begin{split} &\frac{\partial}{\partial t} \left(\rho h \nu_x \right) + \frac{\partial}{\partial x} \left(\rho h \nu_x^2 \right) + \frac{\partial}{\partial y} \left(\rho h \nu_x \nu_y \right) \\ &= \left(\rho - \rho_w \right) g h \sin \alpha_x - 0.5 \frac{\partial}{\partial x} \left\{ \left(\rho - \rho_w \right) g h^2 \cos \alpha_x \right\} + T_x \end{split} \tag{2A}$$

$$\begin{split} &\frac{\partial}{\partial t} \left(\rho h v_y \right) + \frac{\partial}{\partial y} \left(\rho h v_y^2 \right) + \frac{\partial}{\partial x} \left(\rho h v_x v_y \right) \\ &= \left(\rho - \rho_{\rm w} \right) g h \sin \alpha_y - 0.5 \frac{\partial}{\partial y} \left\{ \left(\rho - \rho_{\rm w} \right) g h^2 \cos \alpha_y \right\} + T_y \end{split} \tag{2B}$$

h is the thickness of the current, $v = (v_x, v_y)$ is its velocity, and α_x and α_y are bathymetric slope components in the *x* and *y* directions. The resistance force *T* is taken to be in the turbulent form

$$T = -c_{\rm d}\rho \|v\| v \tag{3}$$

with c_d being the drag coefficient that typically has a value between 0.001 and 0.01 in environmental flows (79). The equations were solved numerically (78) with a time increment of 5 s.

The flow densities were calculated by assuming the suspension of different concentrations of KPT ash particles (ρ_p), the densities of which were taken to be 2300 kg m⁻³. The density of Mediterranean seawater (ρ_w) was taken to be 1030 kg m⁻³. For an equivalent concentration of particles C, the flow density (ρ) is given by

$$\rho = \rho_{\rm p}C + \rho_{\rm w}(1 - C) \tag{4}$$

The currents were run over a 500-m-resolution digital elevation model of the modern seafloor (Fig. 1), modified by removing the KPT accumulations from the Anafi and Amorgos Basins, while also taking into account the fact that these basins have subsided a further ~100 m since the eruption (Fig. 2A). This removal recreates the deep rift basins that existed before the KPT eruption and that served to trap the incoming density currents. Use of the present-day sea-floor bathymetry is subject to some error, because rifting since 161 ka may have modified the bathymetry around Kos (31), but it is a best

first assumption. The ambient seawater layer was assumed to be infinitely high to allow the model to deal with shallow conditions near the eruption source without creating unrealistic conditions. The modeled density currents were never thicker than the local sea depth in the models presented.

We assumed that the density currents were sourced from a cylindrical volume of 30 km in radius, centered on the Kos caldera. We did not attempt to model the very complex transformation of pyroclastic currents into turbidity currents; any thermal effects were ignored, and we assumed that, outside of the source cylinder, the currents were fully water supported. The density currents were generated around the circumference of the source cylinder at an equivalent magma (i.e., virtual suspended solids) flux of $3 \times 10^9 \text{ kg s}^{-1}$ and a supply (i.e., eruption) duration of 24 hours (for a total discharged mass of 2.59×10^{14} kg, equivalent to 108-km³ DRE). The imposed initial velocity of the flows was varied from 0 to 60 m s⁻¹, but the streamline patterns were insensitive to this initial condition because the density currents rapidly adjusted their speeds to the ambient conditions given by the governing equations. Currents of two different densities (1094 and 1157 kg m⁻³, equivalent to 5 and 10 vol % of suspended ash) were modeled, recognizing that these are quite high for the Boussinesq assumption inherent in the depthaveraged model. Flow pathways were imaged by releasing neutrally buoyant tracer particles 6 and 12 hours after the eruption onset. By restricting tracing streamlines to the current body, well behind the leading edge, we avoided complications of modeling the highly unsteady and transient flow fronts. The different models are shown in fig. S2.

Our simple modeling neglects some key processes that occur in natural turbidity currents. First, there is neither a decrease in mass through sedimentation nor an increase through substrate erosion and sediment reentrainment. The flow density remains constant, so the models cannot predict where the density current will lastly stop, except in closed depressions. Neither can the model density currents "ignite" through sediment entrainment (57). The currents just flow to the lowest points in the bathymetry, and, because no deposit forms, there is no modification of the bathymetry with time. Second, the neglect of entrainment of ambient seawater into the currents could also be problematic, because entrainment would slow and thicken the density current, potentially modifying flow pathways. However, the modeling results suggest a posteriori that the no-entrainment assumption is reasonable in this particular case. Water entrainment coefficient is a function (59), $E = 0.075 / (1 + 718 \text{ Ri}^{2.4})^{0.5}$, of the flow Richardson number, $Ri = gh(\rho - \rho_w)/(\rho_w v^2)$. Apart from the frontal region (lasting <1 hour of passage), the flow bodies (thickness of 100 to 200 m; velocity of 1 to 4 m s⁻¹; fig. S2) in our models have Ri in the range of 10 to 100 and are thus subcritical (Ri > 1). This is due to the very low regional bathymetric gradient west of Kos (~0.2°) down which the density currents flow. At such high values of Ri, entrainment rate becomes very low. We, therefore, infer that, while the dynamics of the highly unsteady and transient current head is certainly not captured by our model, the noentrainment assumption may be reasonable for the current body far behind the front. Because the currents are eruption fed for 24 hours, it is the current body that accounts for most of the total transported mass. It is for this reason that we restricted application of the model to the behavior of the quasi-steady current body, with tracer snapshots of the models starting 6 and 12 hours after passage of the front.

Supplementary Materials

This PDF file includes:

Figs. S1 and S2 Tables S1 to S6 References

REFERENCES AND NOTES

- S. Mackie, K. Cashman, H. Ricketts, A. Rust, M. M. Watson, Eds. Volcanic Ash: Hazard observation (Elsevier. 2016).
- A. Freundt, J. C. Schindlbeck-Belo, S. Kutterolf, J. L. Hopkins, Tephra layers in the marine environment: A review of properties and emplacement processes. *Geol. Soc. Lond. Spec. Publ.* 520, 595–637 (2023).
- B. Barone, R. M. Letelier, K. H. Rubin, D. M. Karl, Satellite detection of a massive phytoplankton bloom following the 2022 submarine eruption of the Hunga Tonga-Hunga Ha'apai Volcano. *Geophys. Res. Lett.* 49, e2022GL099293 (2022).
- S. Seabrook, K. Mackay, S. J. Watson, M. A. Clare, J. E. Hunt, I. A. Yeo, E. M. Lane, M. R. Clark, R. Wysoczanski, A. A. Rowden, T. Kula, L. J. Hoffmann, E. Armstrong, M. J. M. Williams, Volcaniclastic density currents explain widespread and diverse seafloor impacts of the 2022 Hunga Volcano eruption. *Nat. Commun.* 14, 7881 (2023).
- G. Iezzi, G. Lanzafame, L. Mancini, H. Behrens, S. Tamburrino, M. Vallefuoco, S. Passaro, P. Signanini, G. Ventura, Deep sea explosive eruptions may be not so different from subaerial eruptions. Sci. Rep. 10. 6709 (2020).
- E. Rossi, G. Bagheri, F. Beckett, C. Bonadonna, The fate of volcanic ash: Premature or delayed sedimentation? *Nat. Commun.* 12, 1303 (2021).
- S. J. Mitchell, K. E. Fauria, B. F. Houghton, R. J. Carey, Sink or float: Microtextural controls on the fate of pumice deposition during the 2012 submarine Havre eruption. *Bull. Volcanol.* 83, 80 (2021).
- M. Jutzeler, M. Manga, J. D. L. White, P. J. Talling, A. A. Proussevitch, S. F. L. Watt, M. Cassidy, R. N. Taylor, A. Le Friant, O. Ishizuka, Submarine deposits from pumiceous pyroclastic density currents traveling over water: An outstanding example from offshore Montserrat (IODP 340). Geol. Soc. Am. Bull. 129, 392–414 (2017).
- S. Carey, H. Sigurdsson, C. Mandeville, S. Bronto, Pyroclastic flows and surges over water: An example from the 1883 Krakatau eruption. *Bull. Volcanol.* 57, 493–511 (1996).
- S. R. Allen, R. A. Cas, Transport of pyroclastic flows across the sea during the explosive, rhyolitic eruption of the Kos Plateau Tuff, Greece. Bull. Volcanol. 62, 441–456 (2001).
- J. Dufek, G. W. Bergantz, Dynamics and deposits generated by the Kos Plateau Tuff eruption: Controls of basal particle loss on pyroclastic flow transport. Geochem. Geophys. Geosystems 8, 10.1029/2007GC001741 (2007).
- J. Dufek, J. Wexler, M. Manga, Transport capacity of pyroclastic density currents: Experiments and models of substrate-flow interaction. J. Geophys. Res. Solid Earth 114, 10.1029/2008JB006216 (2009).
- S. Engwell, J. Eychenne, "Contribution of fine ash to the atmosphere from plumes associated with pyroclastic density currents," in Volcanic Ash (Elsevier, 2016), pp. 67–85.
- S. Kutterolf, A. Freundt, T. H. Druitt, J. McPhie, P. Nomikou, K. Pank, J. C. Schindlbeck-Belo, T. H. Hansteen, S. R. Allen, The medial offshore record of explosive volcanism along the central to eastern Aegean Volcanic Arc: 2. Tephra ages and volumes, eruption magnitudes and marine sedimentation rate variations. Geochem. Geophys. Geosyst. 22, e2021GC010011 (2021).
- R. B. Cole, P. G. Decelles, Subaerial to submarine transitions in early Miocene pyroclastic flow deposits, southern San Joaquin basin, California. Geol. Soc. Am. Bull. 103, 221–235 (1991).
- R. A. F. Cas, J. V. Wright, Subaqueous pyroclastic flows and ignimbrites: An assessment. Bull. Volcanol. 53, 357–380 (1991).
- A. Freundt, Entrance of hot pyroclastic flows into the sea: Experimental observations. Bull. Volcanol. 65, 144–164 (2003).
- J. Trofimovs, L. Amy, G. Boudon, C. Deplus, E. Doyle, N. Fournier, M. B. Hart, J. C. Komorowski, A. Le Friant, E. J. Lock, C. Pudsey, G. Ryan, R. S. J. Sparks, P. J. Talling, Submarine pyroclastic deposits formed at the Soufrière Hills volcano, Montserrat (1995–2003): What happens when pyroclastic flows enter the ocean? *Geology* 34, 549–552 (2006).
- S. R. Allen, A. Freundt, K. Kurokawa, Characteristics of submarine pumice-rich density current deposits sourced from turbulent mixing of subaerial pyroclastic flows at the shoreline: Field and experimental assessment. *Bull. Volcanol.* 74, 657–675 (2012).
- J. C. Schindlbeck, S. Kutterolf, A. Freundt, R. P. Scudder, K. T. Pickering, R. W. Murray, Emplacement processes of submarine volcaniclastic deposits (IODP Site C0011, Nankai Trough). *Mar. Geol.* 343, 115–124 (2013).
- J.T. Gilchrist, A. M. Jellinek, E. E. Hooft, S. Wanket, Submarine terraced deposits linked to periodic collapse of caldera-forming eruption columns. *Nat. Geosci.* 16, 446–453 (2023).
- T. Druitt, S. Kutterolf, T. A. Ronge, C. Hübscher, P. Nomikou, J. Preine, R. Gertisser, J. Karstens, J. Keller, O. Koukousioura, M. Manga, A. Metcalfe, M. McCanta, I. McIntosh, K. Pank, A. Woodhouse, S. Beethe, C. Berthod, S. Chiyonobu, H. Chen, A. Clark, S. DeBari,

- R. Johnston, A. Peccia, Y. Yamanmto, A. Bernard, T. Fernandez Perez, C. Jones, K. B. Joshi, G. Kletetschka, X. Li, A. Morris, P. Polymenakou, M. Tominaga, D. Papanikolaou, K.-L. Wang, H.-Y. Lee, Giant offshore pumice deposit records a shallow submarine explosive eruption of ancestral Santorini. *Commun. Earth Environ.* **5**, 24 (2024).
- M. A. Clare, I. A. Yeo, S. Watson, R. Wysoczanski, S. Seabrook, K. Mackay, J. E. Hunt, E. Lane, P. J. Talling, E. Pope, S. Cronin, M. Ribó, T. Kula, D. Tappin, S. Henrys, C. de Ronde, M. Urlaub, S. Kutterolf, S. Fonua, S. Panuve, D. Veverka, R. Rapp, V. Kamalov, M. Williams, Fast and destructive density currents created by ocean-entering volcanic eruptions. Science 381, 1085–1092 (2023).
- R., Cas, G. Giordano, J. V. Wright, Volcanology. Processes, Deposits, Geology and Resources (Springer, 2024).
- J. Stix, Subaqueous, intermediate to silicic-composition explosive volcanism: A review. Earth Sci. Rev. 31. 21–53 (1991).
- C. W. Mandeville, S. Carey, H. Sigurdsson, Sedimentology of the Krakatau 1883 submarine pyroclastic deposits. *Bull. Volcanol.* 57, 512–529 (1996).
- D. M. Pyle, "Sizes of volcanic eruptions," in The Encyclopedia of Volcanoes (Academic Press, 2015), pp. 257–264.
- O. Bachmann, S. R. Allen, C. Bouvet de Maisonneuve, The Kos–Nisyros–Yali Volcanic Field. Elements 15, 191–196 (2019).
- P. Nomikou, D. Papanikolaou, V. Dietrich, "Geodynamics and Volcanism in the Kos-Yali-Nisyros Volcanic Field," in *Nisyros Volcano*, V. Dietrich, E. Lagios, Eds. (Springer, 2018), pp. 13–55.
- S. R. Allen, Reconstruction of a major caldera-forming eruption from pyroclastic deposit characteristics: Kos Plateau Tuff, eastern Aegean Sea. J. Volcanol. Geotherm. Res. 105, 141–162 (2001).
- G. Pe-Piper, D. J. Piper, C. Perissoratis, Neotectonics and the Kos Plateau Tuff eruption of 161 ka, South Aegean arc. J. Volcanol. Geotherm. Res. 139, 315–338 (2005).
- V. K. Anagnostopoulos, G. Anastasakis, Volcanogenic mass flow deposits and seafloor diapirism following the largest insular Quaternary eruption of the eastern Mediterranean at Nisyros island, Aegean volcanic arc. Mar. Geol. 425, 106185 (2020).
- T. H. Druitt, S. Kutterolf, T.A. Ronge, and the Expedition 398 Scientists. Hellenic Arc Volcanic Field. Proceedings of the International Ocean Discovery Program Expedition Reports, 398 (2024).
- P. Nomikou, C. Hübscher, D. Papanikolaou, G. P. Farangitakis, M. Ruhnau, D. Lampridou, Expanding extension, subsidence and lateral segmentation within the Santorini -Amorgos basins during Quaternary: Implications for the 1956 Amorgos events, central-south Aegean Sea, Greece. *Tectonophysics* 722, 138–153 (2018).
- E. E. Hooft, P. Nomikou, D. R. Toomey, D. Lampridou, C. Getz, M.-E. Christopoulou,
 D. O'Hara, G. M. Arnoux, M. Bodmer, M. Gray, B. A. Heath, B. P. VanderBeek, Backarc tectonism,
 volcanism, and mass wasting shape seafloor morphology in the Santorini-Christiana-Amorgos region of the Hellenic Volcanic Arc. *Tectonophysics* 712-713, 396–414 (2017).
- J. Preine, J. Karstens, C. Hübscher, P. Nomikou, F. Schmid, G. J. Crutchley, T. H. Druitt, D. Papanikolaou, Spatio-temporal evolution of the Christiana-Santorini-Kolumbo volcanic field, Aegean Sea. *Geology* 50, 96–100 (2022).
- T. H. Druitt, L. Edwards, R. M. Mellors, D. M. Pyle, R. S. J. Sparks, M. Lanphere, M. Davies, B. Barreirio, Santorini Volcano. Geol. Soc. Lond. Memoir 19, 165 (1999).
- S. Wulf, J. Keller, C. Satow, R. Gertisser, M. Kraml, K. M. Grant, O. Appelt, P. Vakhrameeva, A. Koutsodendris, M. Hardiman, H. Schulz, J. Pross, Advancing Santorini's tephrostratigraphy: New glass geochemical data and improved marine-terrestrial tephra correlations for the past ~360 kyrs. *Earth Sci. Rev.* 200, 102964 (2020).
- S. Fuller, S. Carey, P. Nomikou, Distribution of fine-grained tephra from the 1650 CE submarine eruption of Kolumbo Volcano, Greece. J. Volcanol. Geotherm. Res. 352, 10–25 (2018).
- O. Bachmann, The petrologic evolution and pre-eruptive conditions of the rhyolitic Kos Plateau Tuff (Aegean arc). Open Geosci. 2, 270–305 (2010).
- F. Lirer, L. M. Foresi, S. M. Laccarino, G. Salvatorini, E. Turco, C. Cosentino, F. J. Sierro, A. Caruso, Mediterranean Neogene planktonic foraminifer biozonation and biochronology. *Earth Sci. Rev.* 196, 102869 (2019).
- Y. Milker, M. F. G. Weinkauf, J. Titschack, A. Freiwald, S. Krüger, F. J. Jorissen, G. Schmiedl, Testing the applicability of a benthic foraminiferal-based transfer function for the reconstruction of paleowater depth changes in Rhodes (Greece) during the early Pleistocene. PLOS ONE 12, e0188447 (2017).
- 43. G. V. Middleton, Experiments on density and turbidity currents: Ill. Deposition of sediment. *Can. J. Earth Sci.* **4**, 475–505 (1967).
- M. Jutzeler, A. S. Clark, M. Manga, I. McIntosh, T. Druitt, S. Kutterolf, T. A. Ronge, Data report: Coring disturbances in advanced piston cores from IODP Expedition 398, Hellenic Arc Volcanic Field in Hellenic Arc Volcanic Field. Proceedings of the International Ocean Discovery Program, 398: College Station, TX (International Ocean Discovery Program, 2025). https://doi. org/10.14379/iodp.proc.398.203.2025.
- O. Bachmann, P. J. Wallace, J. Bourquin, The melt inclusion record from the rhyolitic Kos Plateau Tuff (Aegean Arc). Contrib. Mineral. Petrol. 159, 187–202 (2010).
- C. Bouvet de Maisonneuve, O. Bachmann, A. Burgisser, Characterization of juvenile pyroclasts from the Kos Plateau Tuff (Aegean Arc): Insights into the eruptive dynamics of a large rhyolitic eruption. *Bull. Volcanol.* 71, 643–658 (2009).

SCIENCE ADVANCES | RESEARCH ARTICLE

- M. B. Hart, J. K. Fisher, C. W. Smart, R. Speers, D. Wall-Palmer, Re-colonization of hostile environments by benthic foraminifera: An example from Montserrat, Lesser Antilles Volcanic Arc. Micropaleontology 68, 1 (2021).
- P. J. Talling, M. J. Cartigny, E. Pope, M. Baker, M. A. Clare, M. Heijnen, S. Hage, D. R. Parsons, S. M. Simmons, C. K. Paull, R. Gwiazda, L. Gwyn, J. E. Hughes Clarke, J. Xu, J. R. Silva, K. L. Maier, Detailed monitoring reveals the nature of submarine turbidity currents. *Nat. Rev. Earth Environ.* 4, 642–658 (2023).
- K. V. Cashman, R. S. Fiske, Fallout of pyroclastic debris from submarine volcanic eruptions. Science 253, 275–280 (1991).
- 50. A. H. Bouma, Megaturbidite: An acceptable term? Geo-Mar. Lett. 7, 63–67 (1987).
- E. Keavney, J. Peakall, R. Wang, D. M. Hodgson, I. A. Kane, G. M. Keevil, H. C. Brown, M. A. Clare, M. J. Hughes, Unconfined gravity current interactions with orthogonal topography: Implications for combined-flow processes and the depositional record. Sedimentology 72, 67–99 (2025).
- 52. C. Gladstone, R. S. J. Sparks, The significance of grain-size breaks in turbidites and pyroclastic density current deposits. *J. Sediment. Res.* **72**, 182–191 (2002).
- V. Manville, C. J. N. Wilson, Vertical density currents: A review of their potential role in the deposition and interpretation of deep-sea ash layers. J. Geol. Soc. 161, 947–958 (2004).
- M. Edmonds, R. A. Herd, Inland-directed base surge generated by the explosive interaction of pyroclastic flows and seawater at Soufriere Hills volcano, Montserrat. *Geology* 33, 245–248 (2005).
- K. E. Fauria, M. Manga, Z. Wei, Trapped bubbles keep pumice afloat and gas diffusion makes pumice sink. *Earth Planet. Sci. Lett.* 460, 50–59 (2017).
- 56. R. M. Spratt, L. E. Lisiecki, A Late Pleistocene sea level stack. Clim. Past 12, 1079–1092 (2016).
- G. Parker, Y. Fukushima, H. M. Pantin, Self-accelerating turbidity currents. *J. Fluid Mech.* 171, 145–181 (1986).
- R. M. Dorrell, S. E. Darby, J. Peakall, E. J. Sumner, D. R. Parsons, R. B. Wynn, The critical role
 of stratification in submarine channels: Implications for channelization and long runout
 of flows. J. Geophys. Res. Oceans 119, 2620–2641 (2014).
- H. Ma, G. Parker, M. Cartigny, E. Viparelli, S. Balachandar, X. Fu, R. Luchi, Two-layer formulation for long-runout turbidity currents: Theory and bypass flow case. *J. Fluid Mech.* 1009, A19 (2025).
- A. Polonia, C. H. Nelson, S. C. Vaiani, E. Colizza, G. Gasparotto, G. Giorgetti, C. Bonetti,
 L. Gasperini, Recognizing megatsunamis in Mediterranean deep sea sediments based on the massive deposits of the 365 CE Crete event. Sci. Rep. 12, 5253 (2022).
- 61. D. E. Sawyer, R. Urgeles, C. L. Iacono, 50,000 yr of recurrent volcaniclastic megabed deposition in the Marsili Basin, Tyrrhenian Sea. *Geology* **51**, 1001–1006 (2023).
- S. Shimizu, R. Nakaoka, N. Seama, K. Suzuki-Kamata, K. Kaneko, K. Kiyosugi, H. Iwamaru, M. Sano, T. Matsuno, H. Sugioka, Y. Tatsumi, Submarine pyroclastic deposits from 7.3 ka caldera-forming Kikai-Akahoya eruption. J. Volcanol. Geotherm. Res. 448, 108017 (2024).
- G. Anastasakis, The anatomy and provenance of thick volcaniclastic flows in the Cretan Basin. South Aegean Sea. Mar. Geol. 240, 113–135 (2007).
- C. K. Paull, W. Ussler III, W. S. Holbrook, T. M. Hill, H. Haflidason, W. Winters, T. Lorenson, I. Aiello, J. E. Johnson, E. Lundsten, The tail of the Storegga Slide: Insights from the geochemistry and sedimentology of the Norwegian Basin deposits. *Sedimentology* 57, 1409–1429 (2010).
- J. E. Hunt, Identifying and quantifying erosion beneath the deposits of long-runout turbidity currents along their pathway. Mar. Geol. 389, 32–51 (2017).
- R. S. J. Sparks, R. T. Bonnecaze, H. E. Huppert, J. R. Lister, M. A. Hallworth, H. Mader, J. Phillips, Sediment-laden gravity currents with reversing buoyancy. *Earth Planet. Sci. Lett.* 114, 243–257 (1993).
- P. Nomikou, D. Papanikolaou, M. Alexandri, D. Sakellariou, G. Rousakis, Submarine volcanoes along the Aegean volcanic arc. *Tectonophysics* 597, 123–146 (2013).
- E. Jarosewich, J. A. Nelen, J. A. Norberg, Reference samples for electron microprobe analysis. Geostand. Newslett. 4, 43–47 (1980).
- 69. J. Eychenne, J.-L. Le Pennec, Sigmoidal particle density distribution in a subplinian scoria fall deposit. *Bull. Volcanol.* **74**, 2243–2249 (2012).
- C. Hübscher, M. Hensch, T. Dahm, A. Dehghani, I. Dimitriadis, M. Hort, T. Taymaz, Toward a risk assessment of central Aegean volcanoes. Eos 87, 401–407 (2006).
- J. Karstens, J. Preine, G. J. Crutchley, S. Kutterolf, W. G. M. van der Bilt, E. E. E. Hooft, T. H. Druitt, F. Schmid, J. M. Cederstrøm, C. Hübscher, P. Nomikou, S. Carey, M. Kühn, J. Elger, C. Berndt, Revised Minoan eruption volume as benchmark for large volcanic eruptions. *Nat. Commun.* 14. 2497 (2023).
- I. Raffi, J. Backman, E. Fornaciari, H. Pälike, D. Rio, L. Lourens, F. Hilgen, A review of calcareous nannofossil astrobiochronology encompassing the past 25 million years. *Quat. Sci. Rev.* 25, 3113–3137 (2006).
- K. Perch-Nielsen, "Cenozoic calcareous nannofossils," in *Plankton Stratigraphy*, H. M. Bolli,
 J. B. Saunders, K. Perch-Nielsen, Eds. (Cambridge Univ. Press, 1985), pp. 427–554.

- J. P. Kennett, M. S. Srinivasan, Neogene planktonic foraminifera. A phylogenetic atlas. *Micropaleontology* 265, 546–548 (1983).
- R. Schiebel, C. Hemleben, Planktonic Foraminifers in the Modern Ocean 2020 (Springer-Verlag, 2017).
- I. Raffi, B. S. Wade, H. Pälike, "The Neogene Period," in Geological Time Scale 2020,
 F. M. Gradstein, J. G. Ogg. M. D. Schmitz, G. M. Ogg, Eds. (Elsevier, 2020), pp. 1141–1200.
- F. Cimerman, M. Langer, Mediterranean Foraminifera (Academia Scientiarum et Artium Slovenica Classis, 1991), vol. 30.
- K. Kelfoun, T. H. Druitt, Numerical modeling of the emplacement of Socompa rock avalanche, Chile. J. Geophys. Res. Solid Earth 110, 10.1029/2005JB003758 (2005).
- J. D. Abad, O. E. Sequeiros, B. Spinewine, C. Pirmez, M. H. Garcia, G. Parker, Secondary current of saline underflow in a highly meandering channel: Experiments and theory. *J. Sediment. Res.* 81, 787–813 (2011).
- D. L. Inman, Measures for describing the size distribution of sediments. J. Sediment. Res. 22, 125–145 (1952).
- G. P. L. Walker, Ignimbrite types and ignimbrite problems. J. Volcanol. Geotherm. Res. 17, 65–88 (1983).
- S. N. Carey, H. Sigurdsson, The Roseau ash: Deep-sea tephra deposits from a major eruption on Dominica, Lesser Antilles arc. J. Volcanol. Geotherm. Res. 7, 67–86 (1980).
- M. Jutzeler, J. McPhie, S. R. Allen, Facies architecture of a continental, below-wave-base volcaniclastic basin: The Ohanapecosh Formation, Ancestral Cascades arc (Washington, USA). Geol. Soc Amer. Bull. 126. 352–376 (2014).
- 84. J. V. Wright, E. Mutti, The Dali Ash, Island of Rhodes, Greece: A problem in interpreting submarine volcanigenic sediments. *Bull. Volcanol.* 44, 153–167 (1981).
- R. S. Fiske, T. Matsuda, Submarine equivalents of ash flows in the Tokiwa Formation, Japan. Amer. J. Sci. 262, 76–106 (1964).
- E. Yamada, Subaqueous pumice flow deposits in the Onikobe caldera, Miyagi Prefecture, Japan. J. Geol. Soc. Japan 79, 585–597 (1973).
- A. R. Niem, Mississippian pyroclastic flow and ash-fall deposits in the deep-marine Ouachita flysch basin, Oklahoma and Arkansas. Geol. Soc Amer. Bull 88, 49–61 (1977)

Acknowledgments: This research used samples and data provided by the International Ocean Discovery Program (IODP). We thank the technical staff of the JOIDES Resolution for efforts in attaining the scientific goals of Expedition 398 and all of the shipboard personnel for a great experience. Special gratitude goes to B. Rheinehart, C. Peng, and colleagues in helping us overcome many obstacles and to K. Petronotis and the leadership of IODP for support. We thank the Municipality of Thera for help in preparing for the expedition. Many thanks to Jean-Luc Devidal for expertise in EMPA and LA-ICPMS analysis, to E. Trubert for assistance with mineral preparation and analysis, and to O. Bachmann for providing the onland KPT samples. Helpful reviews from the reviewers improved the manuscript. This is Laboratory of Excellence ClerVolc contribution 678. Funding: We thank the following funding sources: the member organizations of IODP for financing of participation of shipboard scientists on IODP Expedition 398; IODP France for research funding (A.Me. and T.D.); the French Laboratory of Excellence ClerVolc (postdoctoral fellowship of A.Me.); Czech Science Foundation grant 23-06075S (G.K.); Seafloor mapping of Nisyros-Kos region - GEOWARN project contract no: IST-1999-12310 (P.N.): US National Science Foundation grant number OCE-1548026 for seafloor mapping of the Santorini-Amorgos region (P.N.); German Science Foundation DFG grant numbers 434763330 and 506199584 for seismic data processing (C.H. and J.P.); German Research Foundation (DFG) IODP priority programme KU2685/17-1, project number: 527924707 (S.K.); and The International Research Center "Natural disaster and Sustainable development" led by University Clermont Auvergne. Author contributions: Writing—original draft: A.Me., T.D., K.P., S.K., J.P., P.N., C.H., M.Ma., I.M., S.B., K.K., O.K., A.W., and S.C. Writing—review and editing: all authors. Investigation: all authors. Conceptualization: T.D., S.K., C.H., P.N., D.P., and J.P. Project administration: T.A.R. Competing interests: The authors declare that they have no competing interests. Data and materials availability: All data needed to evaluate the conclusions in the paper are present in the paper and/or the Supplementary Materials, including all glass and mineral analyses, grain-size analyses, and microfossil data. High-resolution seismic profiles from cruise POS538 can be accessed from Pangea at https://doi.org/10.1594/ PANGAEA.956579. A selection of vintage seismic profiles can be found in the marine geoscience data system (MGDS) at https://doi.org/10.26022/IEDA/327525 and https://doi. org./10.26022/IEDA/331028. The VolcFlow code can be accessed at https://lmv.uca.fr/volcflow/.

Submitted 5 September 2024 Accepted 15 July 2025 Published 13 August 2025 10.1126/sciadv.ads9642